The Astrophysical Journal Supplement Series, 186:378–405, 2010 February doi:10.1088/0067-0049/186/2/378

THE 22 MONTH *SWIFT*-BAT ALL-SKY HARD X-RAY SURVEY

J. Tueller[1], W. H. Baumgartner[1,2,3], C. B. Markwardt[1,3,4], G. K. Skinner[1,3,4], R. F. Mushotzky[1], M. Ajello[5], S. Barthelmy[1], A. Beardmore[6], W. N. Brandt[7], D. Burrows[7], G. Chincarini[8], S. Campana[8], J. Cummings[1], G. Cusumano[9], P. Evans[6], E. Fenimore[10], N. Gehrels[1], O. Godet[6], D. Grupe[7], S. Holland[1,3], J. Kennea[7], H. A. Krimm[1,3], M. Koss[1,3,4], A. Moretti[8], K. Mukai[1,2,3], J. P. Osborne[6], T. Okajima[1,11], C. Pagani[7], K. Page[6], D. Palmer[10], A. Parsons[1], D. P. Schneider[7], T. Sakamoto[1,12], R. Sambruna[1], G. Sato[13], M. Stamatikos[1,12], M. Stroh[7], T. Ukwata[1,14], and L. Winter[15]

[1] NASA/Goddard Space Flight Center, Astrophysics Science Division, Greenbelt, MD 20771, USA; Wayne.Baumgartner@nasa.gov
[2] Joint Center for Astrophysics, University of Maryland-Baltimore County, Baltimore, MD 21250, USA
[3] CRESST/ Center for Research and Exploration in Space Science and Technology, 10211 Wincopin Circle, Suite 500, Columbia, MD 21044, USA
[4] Department of Astronomy, University of Maryland College Park, College Park, MD 20742, USA
[5] SLAC National Laboratory and Kavli Institute for Particle Astrophysics and Cosmology, 2575 Sand Hill Road, Menlo Park, CA 94025, USA
[6] X-ray and Observational Astronomy Group/Department of Physics and Astronomy, University of Leicester, Leicester, LE1 7RH, UK
[7] Department of Astronomy & Astrophysics, Pennsylvania State University, 525 Davey Lab, University Park, PA 16802, USA
[8] Osservatorio Astronomico di Brera(OAB)/Istituto Nazionale di Astrofisica (INAF), 20121 Milan, Italy
[9] IASF-Palermo/Istituto di Astrofisica Spaziale e Fisica Cosmica di Palermo/Istituto Nazionale di Astrofisica (INAF), 90146 Palermo, Italy
[10] LANL/Los Alamos National Laboratory, Los Alamos, NM 87545, USA
[11] Department of Physics & Astronomy, Johns Hopkins University, 3400 North Charles Street Baltimore, Maryland 21218, USA
[12] Oak Ridge Associated Universities (ORAU), OAB-44, P.O. Box 117 Oak Ridge, TN 37831, USA
[13] Institute of Space and Astronautical Science, JAXA, Kanagawa 229-8510, Japan
[14] Department of Physics/George Washington University (GWU), 2121 I Street, N.W., Washington, DC 20052, USA
[15] Center for Astrophysics and Space Astronomy, University of Colorado, 389 UCB, Boulder, CO 80309, USA
Received 2009 March 17; accepted 2009 November 2; published 2010 January 29

ABSTRACT

We present the catalog of sources detected in the first 22 months of data from the hard X-ray survey (14–195 keV) conducted with the Burst Alert Telescope (BAT) coded mask imager on the *Swift* satellite. The catalog contains 461 sources detected above the 4.8σ level with BAT. High angular resolution X-ray data for every source from *Swift*-XRT or archival data have allowed associations to be made with known counterparts in other wavelength bands for over 97% of the detections, including the discovery of ~30 galaxies previously unknown as active galactic nuclei and several new Galactic sources. A total of 266 of the sources are associated with Seyfert galaxies (median redshift $z \sim 0.03$) or blazars, with the majority of the remaining sources associated with X-ray binaries in our Galaxy. This ongoing survey is the first uniform all-sky hard X-ray survey since HEAO-1 in 1977. Since the publication of the nine-month BAT survey we have increased the number of energy channels from four to eight and have substantially increased the number of sources with accurate average spectra. The BAT 22 month catalog is the product of the most sensitive all-sky survey in the hard X-ray band, with a detection sensitivity (4.8σ) of 2.2×10^{-11} erg cm^{-2} s^{-1} (1 mCrab) over most of the sky in the 14–195 keV band.

Key words: catalogs – galaxies: active – gamma rays: observations – novae, cataclysmic variables – surveys – X-rays: binaries

Online-only material: machine-readable table

1. INTRODUCTION

Surveys of the whole sky that are complete to a well-defined threshold not only provide a basis for statistical population studies but are also a vehicle for the discovery of new phenomena. Compared with lower X-ray energies, where various missions from *Uhuru* (Forman et al. 1978) to *ROSAT* have systematically surveyed the sky and where slew surveys of later missions have added detail, our knowledge of the sky at hard X-rays (>10 keV) has been rather patchy and insensitive. The sensitivity of the HEAO-A4 13–180 keV survey (Levine et al. 1984) was such that only 77 sources were detected.

Recently *INTEGRAL*-IBIS has provided some observations (Bird et al. 2007; Beckmann et al. 2006, 2009; Krivonos et al. 2007) that are much more sensitive but have concentrated on certain regions of the sky; the exposure in the latest IBIS "all-sky" catalog varies from one part of the sky to another by a factor of a thousand, some regions of the sky having only a few thousand seconds of observation. The *RXTE* all-sky slew survey (Revnivtsev et al. 2004) covers much of the sky in the 3–20 keV band and detects 294 sources, but the coverage is not uniform or complete and the sensitivity is weighted to lower energies such that the BAT and *RXTE* sources are not the same.

A survey in the hard X-ray band is important for several reasons. Observations below 15 keV can be drastically affected by photoelectric absorption in certain sources, giving a false indication of their luminosity. Populations of heavily absorbed or Compton-thick active galactic nuclei (AGNs) have been hypothesized in order to explain the portion of the spectrum of the diffuse hard X-ray background ascribed to unresolved sources (Gilli et al. 2007), but such objects have not been found in the necessary numbers, prompting questions as to the composition and evolution of a population of AGNs that could explain its form (Treister et al. 2009). Hard X-ray emission is also being discovered from an unexpectedly large number of previously unknown Galactic sources, notably from certain cataclysmic variables (CVs), symbiotic stars, and heavily obscured high mass X-ray binaries (Bird et al. 2007).

The Burst Alert Telescope (BAT) on *Swift* (Gehrels et al. 2004) has a large field of view and is pointed at a large number of different directions that are well distributed over the sky. The resultant survey provides the most uniform hard X-ray survey to date and achieves a sensitivity sufficient to detect very large numbers of sources, both Galactic and extragalactic. Markwardt et al. (2005) have published the results from the first three months of BAT data, and Tueller et al. (2008) have published a survey of sources seen in the first nine months of *Swift* observations, concentrating on the 103 AGNs seen at Galactic latitudes greater than 15°. We present here a catalog of all sources detected in the first 22 months of operations (2005 December 15–2006 October 27), increasing the number of AGNs to 266 and including all other sources seen across the entire sky.

2. *SWIFT*-BAT

Swift is primarily a mission for the study of gamma-ray bursts (GRBs). *Swift* combines a wide field instrument, BAT, to detect and locate GRBs with two narrow field instruments to study the afterglows: the X-ray Telescope (XRT; Burrows et al. 2005) and the Ultraviolet/Optical Telescope (UVOT; Roming et al. 2005). *Swift*-BAT is a wide field (∼2 sr) coded aperture instrument with the largest CdZnTe detector array ever fabricated (5243 cm^2 consisting of 32,768 4 mm detectors on a 4.2 mm pitch; Barthelmy et al. 2005). BAT uses a mask constructed of 52,000 5 × 5 × 1 mm lead tiles distributed in a half-filled random pattern and mounted in a plane 1 m above the detector array.

This configuration results in a large field of view and a point-spread function (PSF) that varies between 22′ in the center of the field of view and ∼14′ in the corners of the field of view (50° off-axis). When many snapshot images (a snapshot is the image constructed from a single survey observation of ∼5 minutes) are mosaicked together the effective PSF is ∼19′.5.

Point sources are found using a fast Fourier transform convolution of the mask pattern with the array of detector rates; this effectively uses the shadow of the mask cast by a source onto the detector array to create a sky image.

Over much of the BAT field of view, the mask shadow does not cover the whole array. The partial coding fraction is defined as the fraction of the array that is used to make the image in a particular direction and varies across the field of view. The BAT field of view is 0.34, 1.18, and 2.29 sr for areas on the sky with greater than 95%, 50%, and 5% partial coding fractions.

Swift is in low Earth orbit, but because it can slew rapidly it can avoid looking at the Earth. The narrow field instruments cannot be pointed within 45° of the Sun, within 30° of the Earth limb, or within 20° of the Moon.

The pointing plan for *Swift* is optimized to observe GRBs. This strategy produces observations spread out over a few days and at nearly random positions in the sky. The BAT field of view is so large that most of the sky is accessible to BAT on any given day, but the pointing is deliberately biased toward the anti-Sun direction in order to facilitate ground-based optical follow-up observations of GRBs. Even though the *Swift* pointing plan is optimized for GRB observations, BAT's large field of view and *Swift*'s random observing strategy result in very good sky coverage (50%–80% at >20 mCrab in one day) for transients (Krimm et al. 2006).[16] Over a longer term, this observing strategy produces an even more uniform sky coverage (see Figure 1), with an enhanced exposure at the ecliptic poles caused by avoiding the Sun and Moon. This high coverage factor means that the BAT survey can provide reasonably well sampled light curves and average fluxes compiled from data taken throughout the period covered by the survey.

[16] Online at: http://swift.gsfc.nasa.gov/docs/swift/results/transients/

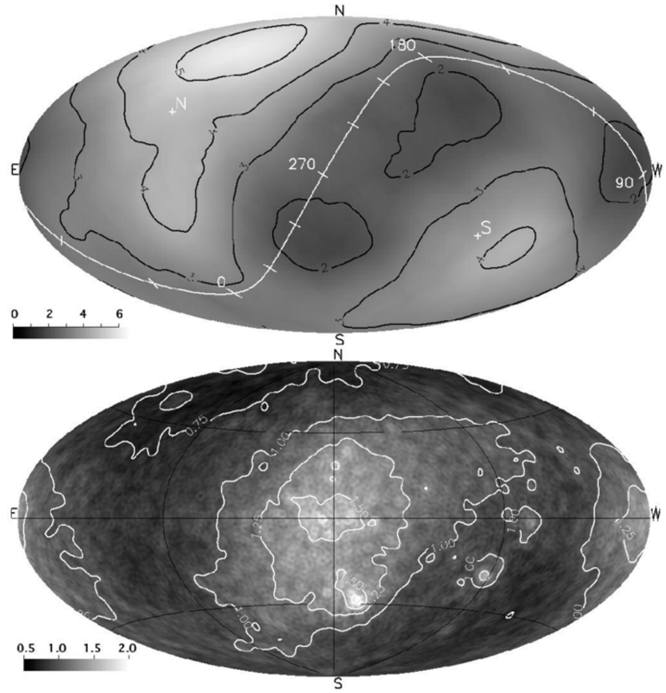

Figure 1. Top panel shows the effective exposure map for the 22-month *Swift*-BAT survey in a Hammer-Aitoff projection on Galactic coordinates. The ecliptic poles and equator are also shown; the largest exposures are toward the north and south ecliptic poles (the units on the color bar are Ms). The bottom panel shows the measured 5σ sensitivity across the sky in units of mCrab in the 14–195 keV band. The bright spots at $l = 344.1$, $b = -44.0$ (GRB060614), $l = 271.8$, $b = -27.2$ (GRB060729), and $l = 254.7$, $b = -1.4$ (GRB060428a) are areas of high systematic noise due to very long exposures (>800 ks) performed early in the mission before dithering in roll angle was instituted.

The effective exposure time of each point in the field of view is the equivalent on-axis time (partial coding fraction times observing time); therefore, the observing time for a place on the sky is generally much larger than is displayed in the effective exposure map. All of the source count rates from the BAT survey are normalized to this effective exposure.

The observing efficiency of *Swift*-BAT is high for a satellite in low Earth orbit, but observing inefficiencies (passages through the South Atlantic Anomaly (SAA) 16%, slewing 16%, down time <1%) still result in a loss of 33% of the total observing time.

The BAT 22 month survey includes data taken between 2004 December 15 and 2006 October 27; there are 39.6 Ms of usable data in the 22 month survey. A typical point on the sky is within the BAT FWHM field of view ∼10% of the time, and the survey data screening rejects 0.5% of the data (see Section 3.1). These two effects result in an effective exposure of 3.9 Ms for a typical point on the sky. The histogram of the effective exposure (Figure 2) shows that most of the sky has an effective exposure time between 1.7 and 4.3 Ms, with a few regions receiving as much as 5.6 Ms.

The BAT PSF is determined by the mask tile cell and detector cell sizes. For an on-axis source, the PSF is approximately Gaussian with an FWHM of 22.5 arcmin. In the native Cartesian tangent plane coordinate system of BAT images, the PSF has nearly a constant shape and size throughout the field of view. However,

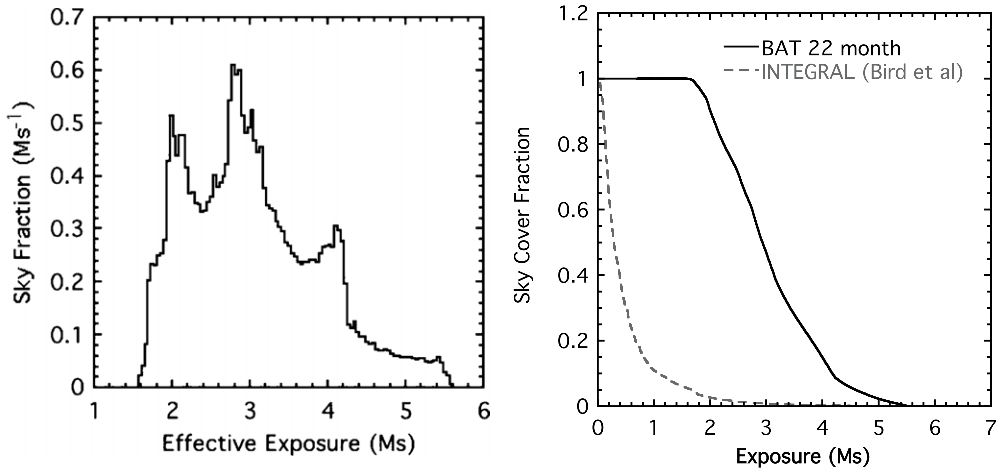

Figure 2. Spatial uniformity in the 22-month BAT hard X-ray survey. The left panel is the effective exposure time histogram (bin size = 40 ks), and the right panel compares the fraction of sky seen by the BAT and *INTEGRAL* surveys as a function of effective exposure times.

because tangent plane units are not spaced at equal celestial angles, the true PSF shape is compressed for off-axis sources, varying approximately as $\sigma_{\rm PSF} = 22\farcm5/(1 + \tan^2\theta)$, where θ is the angle of the source from the pointing axis. When averaged over many pointings, and weighted by partial coding and solid angle, the mean PSF is ∼19.5 arcmin FWHM. We use this 19.5 arcmin PSF when analyzing the BAT survey mosaicked sky maps since they are composed of many contributing snapshot observations.

3. BAT SURVEY PROCESSING

The following sections describe the BAT survey analysis techniques as implemented in the `batsurvey` software tool. General information on coded mask imaging can be found in Skinner (1995, 2008), Fenimore & Cannon (1981), and Caroli et al. (1986).

3.1. BAT Survey Data Collection and Initial Filtering

The BAT instrument monitors the sky in "survey" mode when not within a few minutes of responding to a GRB. In this mode, detected events are binned into histograms by the instrument flight software and the histogram counts are periodically telemetered to the ground (typically on a 5 minute interval). These histograms contain detector (spatial) and pulse height (energy) information. On the ground, the histograms are further adjusted to place all detectors on the same energy scale, and then for the standard survey analysis are re-binned into the eight survey energy bands: 14–20 keV, 20–24 keV, 24–35 keV, 35–50 keV, 50–75 keV, 75–100 keV, 100–150 keV, and 150–195 keV.

Several quality filters are applied to the BAT survey data. First, the spacecraft must be in stable pointing mode, which means that the attitude control "10 arcmin settled" flag must be set. The spacecraft star tracker must be reporting "OK" status, and the boresight direction must be at least 30° above the Earth's limb. Second, BAT must be producing good quality data, which means that the overall array event rate must not be too high or low (3000 counts s^{-1} < rate <12,000 counts s^{-1}); a count rate lower than 3000 counts s^{-1} means that the detector is not operating correctly, and a rate higher than 12,000 counts s^{-1} only occurs during passages through the SAA. A minimum number of detectors must be enabled (>18,000 detectors out of 32,768), and no histogram bins can be reported as missing data because of bad telemetry. In addition, histogram time intervals that cross the UTC midnight boundary are discarded since the spacecraft has at times been commanded to make small maneuvers during that time. These temporal filters produce a set of good time intervals over which the histograms are summed. The finest time sampling of this survey analysis is approximately a single pointed snapshot (which have durations of ∼150–2000 s). The good time intervals are further checked so that the spacecraft pointing does not change appreciably during the interval (1.5 arcmin in pointing, 5 arcmin in roll), and data are excluded if the pointing has varied. Short intervals of 150 s or less are discarded in order to ensure enough counts across the detector for the balancing stage (see Section 3.2) of the processing to work correctly.

After temporal filtering, each pointed snapshot is reduced to a set of eight detector count maps, one for each energy band. Since the systematic noise in the sky images depends on the quality of individual detectors, significant effort is made in optimizing the spatial filtering of the data (i.e., the masking of undesirable detectors). All detectors disabled by the BAT flight software are masked. In addition, the detector counts maps are searched for noisy ("hot") detectors using the `bathotpix` algorithm; any detectors found to be noisy are masked. Finally, detectors with known noisy properties (i.e., high variance compared to Poisson statistics) are discarded. The "fixed pattern" noise (see Section 3.3) is also subtracted from each map.

3.2. Removal of Bright Sources

Bright point sources and the diffuse sky background contribute systematic pattern noise to the entire sky image, at approximately 1% of the source amplitude, due to the coded mask deconvolution technique. By subtracting the contributions of these sources from the detector images, the systematic noise can be significantly reduced. We used the `batclean` algorithm to remove bright sources and diffuse background at the snapshot level. The diffuse background is represented as a smooth polynomial in detector coordinates. Bright sources are represented by the point source response in the detector plane. The source responses are generated using ray tracing to determine the shadow patterns. Bright sources are identified by making a trial sky map, and any point source detected above 9σ in any energy band is marked for cleaning. In our experience—and based on the properties of the BAT mask—no new bright sources become detectable after the batclean calculation, so it is not necessary to iterate the process again. In order to preserve the original bright source intensities, we insert the fluxes from the uncleaned maps into the cleaned maps around the locations of these sources.

At the batclean stage the maps are also "balanced" so that systematic count rate offsets between large-scale spatial regions on the detector are removed. Sources shining through the mask do not produce this kind of coherent structure; therefore this balancing stage helps to remove systematic noise. This process involves dividing the array into detector module sides (128 detectors, [= 16 × 8]), which are separated by gaps of 8.4–12.6 mm from neighboring detector module sides. The mean counts in both the outer edge detectors (44 detectors) and the inner detectors (84 detectors) are subtracted for each module separately, so that the mean rate is as close as possible to zero. Count rate variations from module to module are believed to occur because of variations in the quality of CZT detector material and because of dead time variations in the module electronics caused by noisy pixels. Variations between outer edge and inner detectors in each module are due to cosmic ray scattering and X-ray illumination of detector sides. The BAT coded mask modulates the count rate of cosmic sources on essentially detector-to-detector spatial scales, so the subtraction of the mean count rates averaged over many tens of detectors does not affect the coded signal.

Very bright sources which are partially coded will cast shadows of the mask support structures on the edges of the mask. These shadows are not coded by the mask, are highly energy dependent, and thus must be treated carefully. This is done by masking detectors in regions of the detector plane affected by mask-edge regions for bright sources (∼0.3 Crab or brighter) determined via ray tracing.

After subtracting bright sources and background, detectors whose counts are more than 4σ from the mean are discarded in order to further remove contributions from noisy detectors.

3.3. Fixed Pattern Noise

Non-uniform detector properties cause variations between the background count rates measured in different detectors. These spatial differences form a relatively stable pattern over timescales much longer than a day and are not addressed by the batclean algorithm. These spatial differences also comprise a fixed noise in detector coordinates which is transformed by the survey processing into unstructured noise in the sky image. This fixed pattern is determined by constructing long-term averages of the residual BAT count rates of each individual detector, after subtracting the contributions of bright sources as described above. In this construction, variable terms average to zero and only the stable pattern remains. This pattern maps are then subtracted from each snapshot detector image. The benefit of removing this fixed pattern noise is that each individual detector is addressed, thereby removing systematic noise on a finer scale than the balancing stage mentioned previously.

The contributions of some detectors to this fixed pattern is time dependent as a result of temporal variations in detector performance. We address this time dependence in each detector by fitting a polynomial to the daily average value. The fits are done on data spanning weeks to many months, and the polynomial used has ∼1 order per 30 days fit.

This approach (subtracting the long-term average fixed pattern noise from the data) avoids removing any legitimate signal from sources since *Swift* changes its pointing direction on much shorter timescales.

In practice, the entire survey processing must be run once initially for all of the data, with the pattern contribution set to zero, in order to determine the residual rates mentioned above. Once the pattern maps have been computed, the processing is run a second time using those values.

3.4. Sky Maps

Sky maps are produced for each snapshot using the batfftimage algorithm which cross-correlates the detector count maps with the mask aperture pattern. Sky maps are sampled at 8.6 arcmin on-axis, which corresponds to half the natural element spacing for the coded mask. The natural sky projection for these maps is tangent plane; thus, the sky-projected grid spacing becomes finer by a factor of ∼2 at the extreme edges of the field of view. The angular extent of a sky map from one snapshot covers the region in the sky where the BAT has some non-zero response. This field of view is approximately $120^\circ \times 60^\circ$, although the sensitivity is much reduced at the edges of the field of view due to projection effects through the mask (foreshortening of the mask and shadowing due to the mask thickness at large off-axis angles) and partial coding.

The snapshot maps are corrected for partial coding, geometric projection effects, and the number of active detectors. Thus, they represent the BAT count rate per fully illuminated detector, corrected approximately to the on-axis response. An examination of the measured count rates of the Crab nebula (considered to be a stable point source for the BAT) shows some systematic residual trends as a function of off-axis angle and energy. These effects are primarily due to absorption by passive materials in the field of view, whose absorption lengths scale approximately as $\sec\theta$, where θ is the off-axis angle. The absorptions can be as high as 50% at the lowest energies and largest angles, but are typically smaller. After correction for these effects, the count rate estimates are accurate to within a few percent.

Partial coding and noise maps which represent the partial exposure of each pixel in the sky map are created for each pointed snapshot. The partial coding maps are further adjusted to correct for the fact that some parts of the sky are occulted by the Earth during the observation. For each observation, a map of the average Earth occultation is computed showing the fraction of the observation time each pixel is occulted, and the partial coding map is multiplied by this occultation map to account for the reduced effective observing time. The noise maps are generated by computing the local rms of the pixel values in an annulus around each position (see Section 3.6).

Individual pointed snapshot sky maps are discarded if the differences between the model used in the bright source removal and the cleaned, binned detector plane data lead to a reduced chi-square value greater than 1.25. This filtering excluded primarily data around the bright X-ray source Sco X-1, which produces such strong count rate modulations that they are not reduced to zero at the Poisson statistical level by batclean. This does produce a significant exposure deficit around Sco X-1 and the Galactic center region.

3.5. Mosaicking

The sky images from each snapshot are weighted by inverse variance (i.e., noise^{-2}) and combined into all-sky maps. Each snapshot sky map contributing to the mosaic is trimmed such that all areas of the snapshot have greater than 15% partial coding.

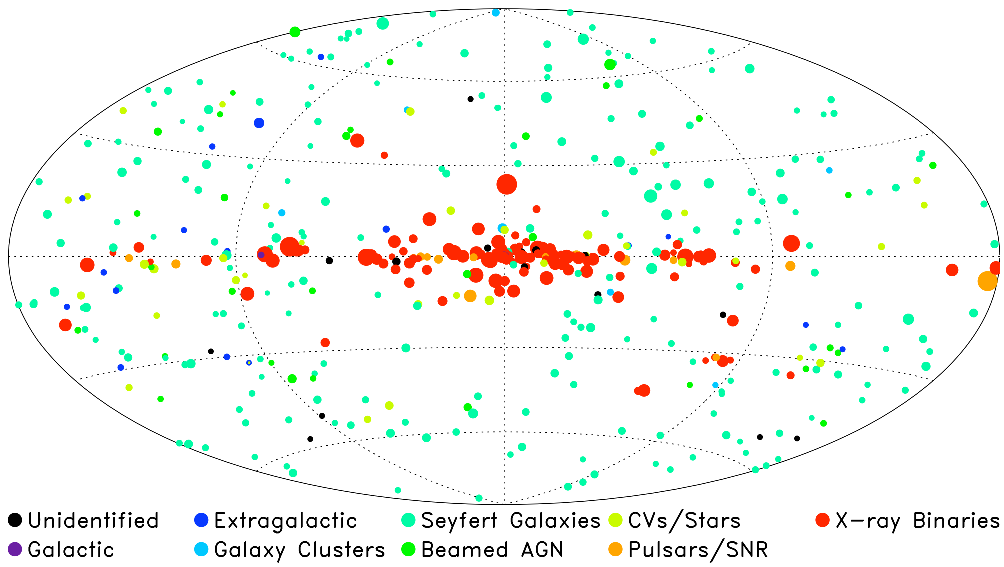

Figure 3. All-sky map showing classification of the BAT 22-month survey sources. The figure uses a Hammer-Aitoff projection in Galactic coordinates; the flux of the source is proportional to the size of the circle. The source type is encoded by the color of the circle.

The sky is divided into six facets in Galactic coordinates, with grid spacing of the pixels 5 arcmin at the center of each facet. The Zenithal Equal Area projection was used in order to minimize distortion far from the center of projection. Each individual sky image is projected and resampled onto the all-sky grids by bilinear interpolation, as are the partial coding and noise maps. The final result is a set of weighted flux maps, propagated noise maps and effective exposure maps for each energy band and facet combination, plus an additional one for the total energy band of 14–195 keV.

This analysis procedure produces a sky image where each pixel represents the best estimate of the flux for a point source at the corresponding position in the sky (see Fenimore & Cannon 1981 for more information on coded mask image reconstruction).

3.6. Source Detection

A "blind" source detection algorithm was used to search for sources in the mosaicked significance maps using the full survey bandpass of 14–195 keV. The significance map is the ratio of the counts map to the local noise map.

The rms noise map is calculated from the mosaicked sky map using an annulus of radius 30 pixels (2°.5) with an inner exclusion radius of 8 pixels (40′). An 8 pixel radius around the position of all known BAT sources is also excluded from the regions used for background calculation. We do not attempt to fit the PSF of the source for the noise calculation and hence the positions of sources must be eliminated from this calculation to get an accurate measure of the underlying noise in the image.

The noise is assumed to be a smooth function of image position and so the value at the center of the annulus is well approximated by the average value in the annulus. This calculated noise includes both statistical and systematic noise and is therefore a better estimate of the total noise in the image than the noise calculated from a PSF fit. The noise from every source is distributed over the whole image, just as the signal from the source is distributed over the detector array, so no local enhancement of noise at the position of the source is expected.

The blind search algorithm first finds all peaks in the map by searching for pixels that are higher than each of the surrounding 8 pixels. If the significance in a peak pixel is greater than our detection threshold of 4.8σ (see Section 4.4), the excess is considered to be a detection in the blind search for new sources.

4. THE *SWIFT*-BAT 22-MONTH CATALOG

The catalog of sources detected by *Swift*-BAT using the first 22 months of data includes sources at all Galactic latitudes. The 22-month catalog and associated data in electronic form can be found online at the *Swift* Web site.[17]

Figure 3 shows the distribution of sources on the sky color coded by source type, with the symbol size proportional to the source flux in the 14–195 keV band. Table 1 gives the distribution of objects according to their source type. Sources classified as "unidentified" are those where the physical type of the underlying object (e.g., AGN, CV, XRB, etc.) is unknown. These sources have a primary name derived from the BAT position. Some unidentified BAT sources are associated with sources in the X-ray or gamma-ray bands (with positions unable to sufficiently determine an optical counterpart or physical source type), and these sources can be distinguished by having a name in the catalog derived from the observation in the other waveband. The few sources classified only as "Galactic" generally lie in the plane and have shown some transient behavior which indicates a Galactic source, but no other information is available that would allow further classification. "Extragalactic" sources are detected as extended sources in optical or near-IR imaging, but do not have other indications of being an AGN. The "Beamed AGN" category includes BL Lacs, blazars, and FSRQs.

Table 5 is the listing of all the sources detected above the 4.8σ level in a blind search of the 22-month *Swift*-BAT survey maps. The first column is the source number in the 22-month catalog. The second column of the table is the BAT name, constructed from the BAT source position given in columns 3 and 4. In cases where the source have been previously published with a BAT name corresponding to a slightly different location (e.g., a source position from a previous BAT catalog with less data), we have used the first published name but have given the correct 22-month BAT coordinates in columns 2 and 3. The fifth column

[17] http://swift.gsfc.nasa.gov/docs/swift/results/bs22mon/

Table 1
Counterpart Types in the *Swift*-BAT 22-month Catalog

Class	Source Type	No. in Catalog
0	Unidentified[a]	18
1	Galactic [b]	3
2	Extragalactic[c]	13
3	Galaxy Clusters	7
4	Seyfert Galaxies	234
5	Beamed AGN[d]	32
6	CVs/Stars	36
7	Pulsars/SNR	15
8	X-ray Binaries	121

Notes.
[a] Sources listed as unidentified either do not have any known counterpart, or are associated with sources of unknown physical type.
[b] Sources classified as galactic are so assigned because of observed transient behavior in the X-ray band along with insufficient evidence to place them in another class.
[c] Sources in the extragalactic class are seen as extended in optical or near-IR imagery, but do not have firm evidence (such as an optical spectrum) from other wavebands confirming whether they harbor an AGN.
[d] Sources classified as "beamed AGN" include blazars, BL Lacs, FSRQs, quasars, and other high-redshift AGNs.

is the significance of the blind BAT source detection in sigma units. Instances where more than one possible counterpart to a single BAT source is likely are indicated with ditto marks in Columns 2–5.

The sixth column gives the name of the identified counterpart to the BAT hard X-ray source with the most precisely known position. These are often optical galaxies, or Two Micron All Sky Survey (2MASS) sources, and are associated with a source detected in the medium-energy X-ray band (3–10 keV) in *Chandra*, *XMM-Newton*, or XRT images. Counterpart determination is discussed in Section 4.2. The seventh column gives an alternate name for the counterpart. We have preferred to list a well-known name (e.g., Sco X-1) or a name from a hard X-ray instrument or high energy detection. The best available coordinates of the counterpart (J2000) are given in the table in Columns 8 and 9.

The 10th and 11th columns give the 14–195 keV flux of the BAT source (in units of 10^{-11} erg s^{-1} cm^{-2}) and its 1σ error. The BAT flux for each counterpart is extracted from the hard X-ray map at the location of the counterpart given in Columns 8 and 9. The flux determination method is described in Section 4.5.

The 12th column indicates whether there is source confusion: there is source confusion either if there is more than one possible XRT counterpart or if two likely hard X-ray sources lie close enough together to make a proper extraction of the flux not possible with the standard method. The treatment of confused sources is discussed in more detail in Section 4.3. We define two classes of source confusion: "confused" sources, and "confusing" sources. A source is "confusing" for the purposes of this column if a fit to the map indicates that the source contributes to the hard X-ray flux of a neighboring source. A "confused" source has received more than 2% of its flux from a neighboring source. A confused source is labeled with an "A" in this column, and a confusing source with a "B" (the case of a very bright source next to a weak one would result in the bright source labeled with a "B" and the weak source with an "A"). A source that is both confused and confusing (e.g., the case where there are two similar strength sources close to each other, such as when there are two possible XRT counterparts to a single BAT source) is labeled with an "AB."

When a source has an entry in Column 12, a best estimate of the counterpart flux is listed in Column 10 from a simultaneous fit of all the counterparts in the region to the BAT map. When the entry is "A" or "AB" in Column 12 (indicating a confused source), the error on the flux is not well defined, and Column 11 is left blank. (See Section 4.5).

The 13th and 14th columns list the source hard X-ray hardness ratio and its error computed as described in Section 4.7. The hardness ratio is defined here as the ratio of the count rate in the 35–150 keV band divided by the count rate in the 14–150 keV band.

The 15th and 16th columns give the redshift and BAT luminosity of the counterpart if it is associated with a galaxy or an AGN. The source luminosity (with units log[erg s^{-1}] in the 14–195 keV band) is computed using the redshift and flux listed in the table and a cosmology where $H_0 = 70$ km s^{-1} Mpc^{-1}, $\Omega_m = 0.30$, and $\Omega_\Lambda = 0.70$.

The 17th column lists a source type with a short verbal description of the counterpart.

4.1. Source Positions and Uncertainties

The BAT position is determined by using the BAT public software tool `batcelldetect` to fit the peak in the map to the BAT PSF (a two-dimensional Gaussian with an FWHM of 19.5 arcmin). The `batcelldetect` program performs a least-square fit using the local rms noise to weight the pixels in the input map. These fit positions were used to generate the BAT positions in the catalog and the names of newly detected BAT sources.

The PSF fit using `batcelldetect` also reports a formal position uncertainty based on the least-square covariance matrix. However, because neighboring pixels in the coded mask images are inherently correlated, the formal uncertainty reported by this technique will not be representative of the true uncertainty. Therefore we choose to use the offset between the fit position and the counterpart position as an indicator of the BAT position error.

The `batcelldetect` program also has the option of fitting source locations using an input catalog of starting positions. We have used this capability to test the stability of the source positions found by `batcelldetect` by using an input catalog where all the starting positions have been offset by 8 arcmin in a random direction from the source position found in the blind search. We have performed this test with several different offsets and find that the fit converges to within 1 arcmin of the counterpart position for BAT sources that are not confused. For a few sources, the fit sometimes converges onto a side peak instead of the primary peak, but this error is not repeated in additional tests starting from other randomized positions. This type of systematic error in the position determination does not occur in the blind search (Section 3.6) since we use the maximum pixel to start the fit instead of a randomized spot 8 arcmin from the blind position. Anomalous offsets in the source position are identified by examination of the image and refitting.

In order to judge the accuracy of the BAT positions, we plot in Figure 4 the angular separation between the BAT position and the counterpart position against the significance of the BAT source detection. The accuracy of the BAT position improves as the significance of the detection becomes stronger. There are 461 BAT sources in Table 5 with detection significances greater than

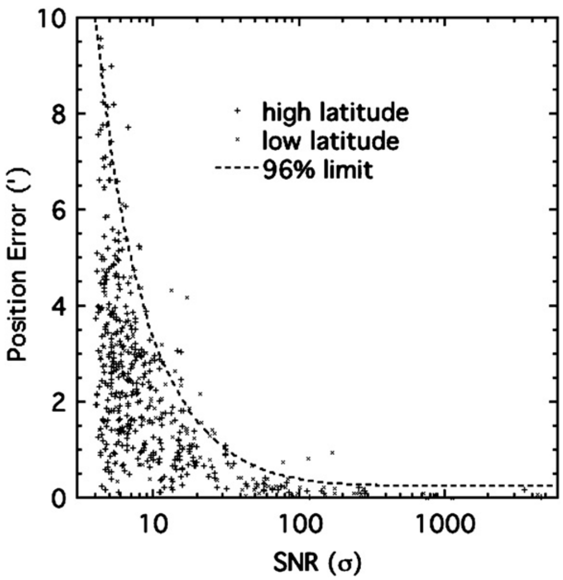

Figure 4. BAT position error as a function of the BAT detection significance. The angular separation between the counterpart position and the fitted BAT position is used to determine a measured position error for each source. This measured position error is plotted as a function of BAT detection significance. The dashed line in the plot shows the 96% error radius as a function of BAT source detection significance. Sources with large position errors are almost always low galactic latitude sources falling in regions of high source density and locally higher noise.

4.8σ; there are 479 possible counterparts, and of these 25 are located grater than 5 arcmin from the BAT position. Therefore, there is only a ~5% chance of a BAT-detected source ($>4.8\sigma$) having a counterpart farther away than 5 arcmin.

In Figure 4, we also plot a line showing our estimate of the BAT position error for a given source significance. This estimate for the error radius (in arcminutes) can be represented with the function

$$\text{BAT error radius} = \sqrt{\left(\frac{30}{(\mathrm{S/N}-1)}\right)^2 + (0.25)^2}, \quad (1)$$

where S/N is the BAT detection significance. This empirical function includes a systematic error of 0.25 arcmin deduced from the position errors of very significant sources. This error radius includes 96% of the sources that are greater than 5° from the Galactic plane and 15° from the Galactic center. The error radius encloses 85% of sources in the Galactic plane. Sources known to be confused are not included in the plot.

4.2. *Counterparts*

Counterparts to the BAT sources were primarily discovered by examining X-ray images taken with instruments with good angular resolution. *Chandra* resolution is sometimes required on the plane, otherwise *XMM-Newton*, Suzaku, or ASCA images were examined. *ROSAT* images and source catalogs were of relatively low importance for counterpart identification because of *ROSAT*'s lack of effective area in the hard X-ray band, because of the poor correlation between *ROSAT* flux and the BAT hard X-ray flux (see Tueller et al. 2008, Figure 7), and because of the high chance probability of finding a *ROSAT* source in the BAT error circle.

If no archival X-ray images existed for the location of a BAT source, we requested *Swift*-XRT follow-up observations of the field containing the BAT source. A 10 ks observation with XRT is deep enough to detect almost all BAT sources. BAT extragalactic sources are usually AGNs contained in bright ($J \sim 13$), nearby galaxies at redshift $z < 0.1$ and are easily identified in an XRT observation.

The X-ray counterpart to an unabsorbed BAT source is a very bright XRT source, which is easily detected with a 2 ks XRT observation. However, most of the new BAT sources are heavily absorbed in the X-ray band and were not detected by *ROSAT*. We have found empirically that XRT can detect essentially all of the BAT sources (including the absorbed ones) in a 10 ks observation.

We require consistency of the BAT and the X-ray spectrum (>3 keV) when simultaneously fit with an absorbed power law allowing only a renormalization between BAT and XRT to account for variability. This consistency of the spectra is required for all sources not previously known to be hard X-ray emitters, except transients and sources known to have highly variable spectra where the BAT spectrum averaged over years cannot be directly compared to the XRT measurement from a single observation.

A small fraction of XRT follow-up observations in the 5–10 ks range detected multiple sources consistent with the BAT position. In these cases, the counterpart to the BAT source was almost always identified by limiting the bandpass of the X-ray image to the higher energy 3–10 keV band. This bandpass filtering usually reduced the number of sources in the field to a single hard source.

In the few cases where two or more hard sources still remain after bandpass filtering, all are considered possible counterparts to the BAT source and listed in the catalog with a flag indicating that the counterpart identification suffers from source confusion. There are 18 more possible counterparts in Table 5 than there are blind BAT sources (461) because of the 15 cases where there are one or more possible counterparts to a single BAT source.

Because the counterpart identification requires an X-ray point source with a small error radius (~4 arcsec), a positional coincidence with a known source or bright galaxy, and an X-ray spectrum consistent with the BAT flux, we believe that the counterpart misidentification rate is extremely small. All of the identified counterparts listed in Table 5 are hard X-ray sources.

4.3. *Confused Sources*

Sources are labeled as confused in our table when the highest pixel associated with the BAT source in the mosaicked maps (the "central pixel" value) has a significant contribution from adjacent sources. This includes the cases when two possible X-ray counterparts lie within a single BAT pixel and when two BAT sources are close enough that each contributes flux to the location of the adjacent source.

Using the positions of the X-ray counterparts as an input catalog, we calculated the fractional contribution of each BAT source to its neighbors. We used the significance measured in the blind search and the 19.5 arcmin FWHM Gaussian BAT PSF to calculate the intensity of each source at the position of its neighbors. The central pixel value for each BAT source was assumed to be the sum of the source plus all the contributions from its neighbors. This creates a set of linear equations that can be solved for the true significance of each source. We solved these equations with the constraint that sources were not allowed to have negative significance. This procedure was devised to determine cases where the BAT significance

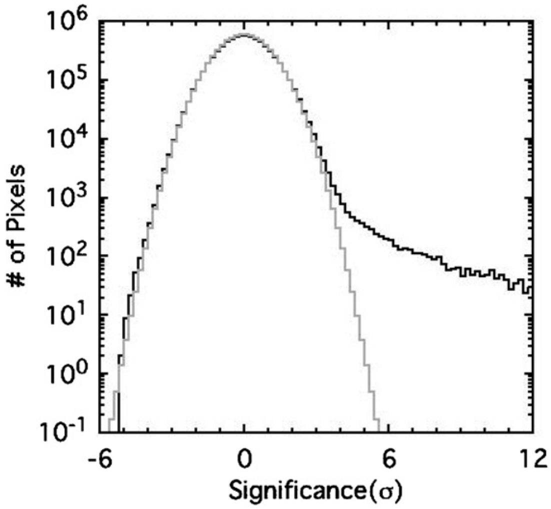

Figure 5. Histogram showing the significances of the pixels in the 22-month survey. The gray line is not a fit to the data; it is a Gaussian distribution with $\sigma = 1$ and normalized to the peak of the observed distribution.

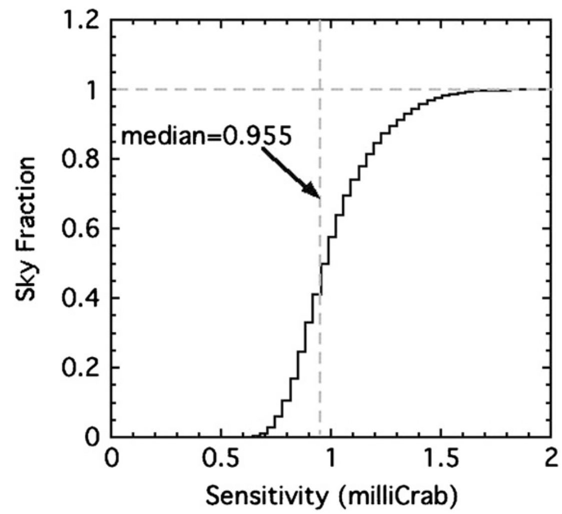

Figure 6. Integral distribution of sky coverage versus sensitivity achieved in the survey. The 1 mCrab sensitivity limit (for 50% sky coverage) corresponds to a flux of 2.3×10^{-11} erg cm^{-2} s^{-1} in the 14–195 keV band.

is altered because of the presence of a very strong nearby source.

If we found that the resulting fit S/N from the technique that accounted for contributions from neighbors was lower than the central pixel S/N from the blind search by 2%, we labeled it as confused.

4.4. Detection Significances and Limits

The detection significance for the BAT sources in the catalog is extracted from the mosaicked significance map at the BAT position (see Section 3.6). The significance is taken from the highest pixel value in the blind search.

Figure 5 shows the distribution of individual pixel significances from the mosaicked map of the entire sky. As is usual for a coded mask imager, the noise distribution is a Gaussian function centered at zero significance, with a width of $\sigma = 1$ and a total integrated area equal to the number of pixels in the map. The large tail at positive significance is due to real astrophysical sources present in the map.

The distribution of the pixel significances in Figure 5 closely follows a Gaussian distribution for the negative significances. The positive side of the distribution also follows a Gaussian, but with the addition of pixels with enhanced significances because of the presence of real sources in the map.

Examination of the negative fluctuations provides a good measure of the underlying noise distribution. There is only 1 negative pixel in the entire map with a magnitude greater than 5σ. We therefore choose our detection limit to be 4.8σ. This detection limit is also the same as used in the 9-month version of the *Swift*-BAT catalog. While it is clear that there are several real sources with significances somewhat smaller than 4.8σ, we choose this value in order to minimize false sources caused by random fluctuations. We expect random fluctuations to account for 1.54 sources at the 4.8σ level in our sky map of 1.99×10^6 independent pixels.

Figure 6 shows the integral distribution of sky coverage versus sensitivity achieved in the survey. We achieve a sensitivity of better than 1 mCrab for half the sky, which corresponds to a flux of $<2.3 \times 10^{-11}$ erg cm^{-2} s^{-1} in the 14–195 keV band.

4.5. Counterpart Fluxes

Fluxes of the counterparts to BAT sources were extracted from the mosaicked maps using the pixel containing the position of the identified counterpart. For sources where a counterpart is not known, we use the fitted BAT position to determine the flux.

We have chosen to normalize source fluxes in the eight survey bands to the Crab because the systematic uncertainties in the survey averaged Crab spectrum are smaller than the uncertainties in the BAT survey response matrix. The source fluxes in each band were computed by comparing the source count rate to the measured rate of the Crab Nebula in each band:

$$\text{BAT source flux} = \left(\frac{\text{BAT source count rate}}{\text{Crab count rate}}\right) \text{Crab flux}, \quad (2)$$

where the Crab flux in each band is given by

$$\text{Crab flux} = \int_a^b E\ F(E)\, dE, \quad (3)$$

where a and b are the lower and upper BAT band edges and E the energy in keV.

We take the Crab counts spectrum to be

$$F(E) = 10.17\ E^{-2.15} \left(\frac{\text{photons}}{\text{cm}^2\ \text{s keV}}\right), \quad (4)$$

determined by fitting a power-law model to BAT on-axis calibration observations taken early in the *Swift* mission. These values are consistent with characterizations of the Crab spectrum using data from Integral/SPI (Jourdain & Roques 2008), Integral/IBIS (Jourdain et al. 2008), HETE/FREGATE (Olive et al. 2003), SAX/PDS (Fiore et al. 1999), and GRIS (Bartlett 1994).

The total Crab flux is then

$$\text{Crab flux} = \int_{14\ \text{keV}}^{195\ \text{keV}} E\ F(E)\, dE = 2.44 \times 10^{-8} \left(\frac{\text{erg}}{\text{cm}^2\ \text{s}}\right). \quad (5)$$

Sources with a spectral index very different from the Crab can have a small but significant residual systematic error in the fluxes determined with this method.

In order to gauge this error we generated counts spectra for different models in the eight survey bands using the BAT on-axis spectral response matrix. The Crab comparison flux determination method described above was used to obtain the model fluxes in each of the eight survey bands. The flux errors between the computed fluxes and the model fluxes in the individual bands were always $<10\%$ for a range of model spectral indices between 1 and 3 and so we deem this technique acceptable for producing the source fluxes in each of the survey bands.

We fit the 8-channel spectra with a power-law model in order to produce an overall hard X-ray flux for each BAT source. We used `XSPEC` and a diagonal matrix to fit the 8-channel spectra with the `pegpwrlw` model over the entire 14–195 keV BAT survey energy range in order to extract the source flux in this band. This approach was selected because it weights the energy bands by their individual uncertainties; a simple sum of the bands would produce a very large error due to the high weight it assigns to the noisiest bands at the highest energies.

The 1σ error in the overall flux was determined by using the error function in XSPEC and is given in Table 5. For the highest significance BAT sources ($>100\sigma$), this procedure does not produce a good fit (reduced $\chi^2 \gg 1$), but this is to be expected from the very high significances of each point and the coarse energy binning. To evaluate the systematic error in the fitting we performed fits to our model spectra generated from the response matrix. For power-law spectra, the systematic error in the flux is dominated by the error in the individual data points as calculated above. Sources with hardness ratios less than 0.1 are not well fitted with a power law, and the systematic uncertainty in the flux can be significantly larger.

The fluxes for sources marked as confused were calculated in a slightly different way. Instead of using the count rate extracted from the map at the counterpart position, we performed a simultaneous fit to find the fluxes of all the sources in the confused region as described in Section 4.3. For these sources we do not quote an error on the flux estimate because the behavior of the errors with this fitting technique is not well known. Any source with a confused flag should be considered as detected by BAT but the flux should be considered as an upper limit.

4.6. Sensitivity and Systematic Errors

In this section, we compare the expected statistical errors with the actual measured statistical noise in the final mosaic maps. From the perspective of pure Poisson counting statistics, the uncertainties are governed primarily by the properties of the coded mask and the background (see Skinner 2008 for details). The expected 5σ noise level can be expressed as (adapting from Skinner 2008 Equations (23) and (25)):

$$5\sigma_{\rm Poisson} = 5\sqrt{\frac{2b}{\alpha\, N_{\rm det}\, T}}, \tag{6}$$

where b is the per-detector rate, including background and point sources in the field of view; $N_{\rm det}$ is the number of active detectors ($N_{\rm det} \leqslant 32768$); T is the effective on-axis exposure time; and α is a coefficient dependent on the mask pattern and detector pixel size ($\alpha = 0.733$ for BAT). The partial coding, p, enters the expression through the "effective on-axis exposure" time, $T = pT_o$, where T_o is the actual exposure time. Using nominal values ($b = 0.262$ counts s^{-1} detector^{-1}; $N_{\rm det} = 23{,}500$ (the exposure-weighted mean number of enabled detectors); and Crab rate $= 4.59 \times 10^{-2}$ counts s^{-1} detector^{-1}), we find the estimated Poisson 5σ noise flux level to be

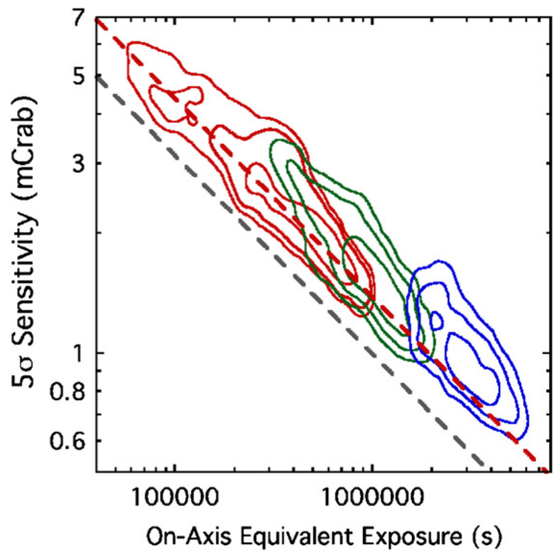

Figure 7. Measured 5σ BAT sensitivity limit for pixels in the all-sky map, as a function of effective exposure time, T, for the 3-month (red; Markwardt et al. 2005), 9-month (green; Tueller et al. 2008), and 22-month (blue; this work) survey analyses. The contours indicate the number of pixels with a given sensitivity and effective exposure. The contour levels are linearly spaced. The red dashed line represents the original $T^{-1/2}$ sensitivity curve quoted in Markwardt et al. (2005). The black dashed line represents a lower limit to the expected Poisson noise level (see Section 4.6). The measured noise is approximately 30%–45% higher than the expected Poisson noise.

$$f_{5\sigma} = 0.99\ {\rm mCrab}\left(\frac{T}{1\ {\rm Ms}}\right)^{-1/2}. \tag{7}$$

We consider this to be a lower limit to the expected Poisson noise level for a given effective exposure. In reality, the background rate b may be higher than the nominal value by up to 50% depending on the particle environment of the spacecraft. Also, along the Galactic plane the contributions of bright sources, such as the Crab, Sco X-1, and Cyg X-1, are not strictly negligible, and will raise the overall level of b by up to $\sim$10%. All of these adjustments would cause a Poisson noise level larger than given by Equation (7), by an amount that depends on the specific satellite conditions during the survey. We estimate that, averaged over the entire survey duration, the true Poisson noise level may be 5%–15% higher than the lower limit quoted above.

Figure 7 compares the measured noise and expected noise versus effective on-axis exposure. We see that both noise measures are decreasing approximately as $T^{-1/2}$, which suggests that the dominant errors are uncorrelated over time. It also suggests that pointing strategies such as roll-angle dithering have been successful in reducing pointing-related systematic errors. However, the measured noise is still higher than the expected Poisson noise by $\sim$30%–45%, and we take this to be a measure of the unmodeled systematic variations on the detector plane.

The largest likely contributors to systematic variations are improper subtractions of diffuse background, and of bright sources. BAT count rates are background-dominated—the background rate is equivalent to $\sim$6–9 Crab units—so the coded mask analysis is particularly sensitive to imperfect subtraction of spatial background variations. While the pattern map method and the functions fitted during the cleaning stage produce a good model of the detector background, some imperfections remain. One

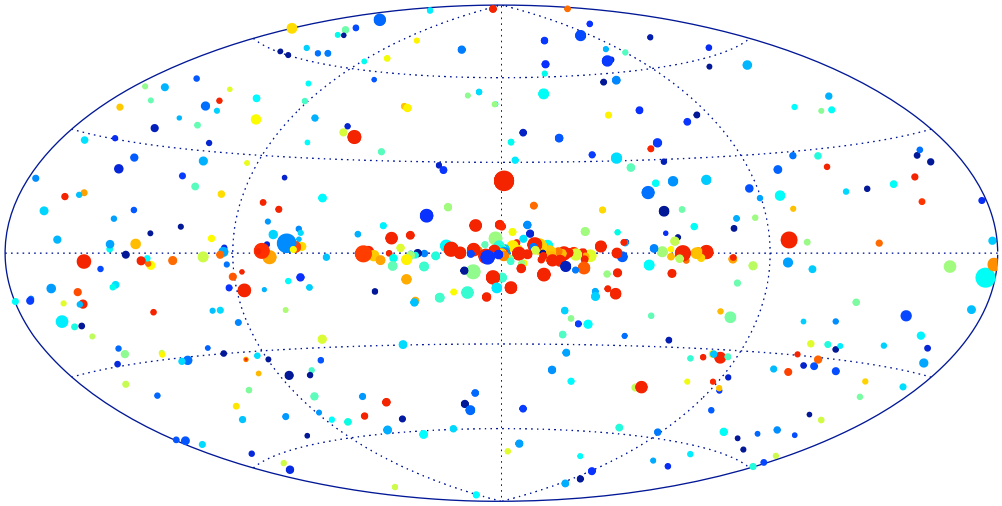

Figure 8. All-sky map showing spectral hardness of BAT 22-month survey sources. The figure uses a Hammer-Aitoff projection in Galactic coordinates; the size of the circle is proportional to the flux of the source. Blue sources are harder, and red sources are softer.

effect is that detector-to-detector sensitivity differences, coupled with varying exposures to the X-ray background, can lead to excess residuals.

For similar reasons, bright sources may also contribute systematic noise. The brightest sources are clustered along the Galactic plane, and thus contribute noise in those preferred locations. Indeed, we note that the measured noise is ∼50% higher in the Galactic center region, where there is a concentration of bright point sources. This is a larger factor than can be accounted for by a larger count rate. Modeling of point sources may be imperfect for the same reasons as for the background. Also, there may be other effects such as side illumination of detectors that may contribute additional noise. Here, "side illumination" refers to the facets of the individual CdZnTe detectors which do not face the pointing direction, but are still sensitive to X-rays. Off-axis sources will shine through the mask and illuminate the sides, producing an additional (although fainter) coded signal. At the moment, illumination of the sides of detectors is not modeled at the imaging or cleaning steps, and thus there will be an additional noise due to the effect.

Proper modeling of these systematic error contributors will be the subject of future work. At this stage we do not have an in-depth analysis of the quantitative contributions of each effect to the systematic noise, and in some cases the analysis may be prohibitively difficult. Still, at the current exposure levels, the noise level seems to be decreasing with exposure, and we do not appear to be reaching an ultimate systematic limit in this analysis.

4.7. Spectral Analysis

In Section 4.5, we use a simple power-law fit to the data to estimate the source flux. However, because the catalog contains sources with various different physical natures and spectral shapes, we choose to use the more robust characterization given by a hardness ratio to describe the BAT spectra.

Hardness ratios for the *Swift*-BAT sources were calculated by taking the sum of the count rate in the 35–150 keV band and dividing by the count rate in the 14–150 keV band. Errors on the hardness ratio were calculated by propagating the errors on the count rates in the individual eight bands except when the source is listed as confused. Figure 8 shows a map of the source positions on the sky, with the source flux represented by the size of the point and the source hardness by the color (red is softer and blue is harder). Figure 9 shows the hardness ratios of the 22-month BAT sources by source class.

A mapping can be made between hardness ratio and power-law index for sources that have spectral shapes well described by a simple power-law model (e.g., the majority of AGNs in our catalog). This mapping is well represented by

$$\Gamma = 3.73 - 4.52\ \mathrm{HR}, \qquad (8)$$

where Γ is the power-law index and HR is the hardness ratio as defined above. Figure 10 shows the correlation between power-law index and hardness ratio for the BAT survey sources. The correlation holds well for sources with hardnesses above about 0.15, but begins to break down for softer sources. An illustration of this problem is the soft BAT spectra of clusters of galaxies, which have thermal spectra with temperatures ∼10 keV and are usually detected only in the lowest energy BAT band and are not well fitted by a power-law model. We leave to a later paper a more careful spectral analysis using models appropriate for the physical nature of the sources.

5. *SWIFT*-BAT SURVEY SOURCES

Although it is for extragalactic astronomy that the present survey represents the greatest step forward, a comparison of the results for Galactic sources with earlier work also has interesting implications.

Of the 479 sources in Table 5, 97% have reasonably firm associations either with objects known in other wavebands or with previously known X-ray or gamma-ray sources. More than 60% of the associations are with extragalactic objects. At high Galactic latitudes ($|b| > 10°$) the density of identified extragalactic sources is 22.6 sr^{-1}, and it is only slightly reduced at low latitudes to 19.2 sr^{-1}. This suggests that only ∼ seven extragalactic sources in the plane are missed through reduced sensitivity, lack of information in other wavebands, or confusion, and illustrates the uniformity of the survey.

153 BAT AGNs were previously reported in the BAT 9-month AGN survey (Tueller et al. 2008). Winter et al. (2009) provide X-ray spectral fits for these sources and provide measures of the luminosity, n_{H} etc. for the sources in the 9-month catalog.

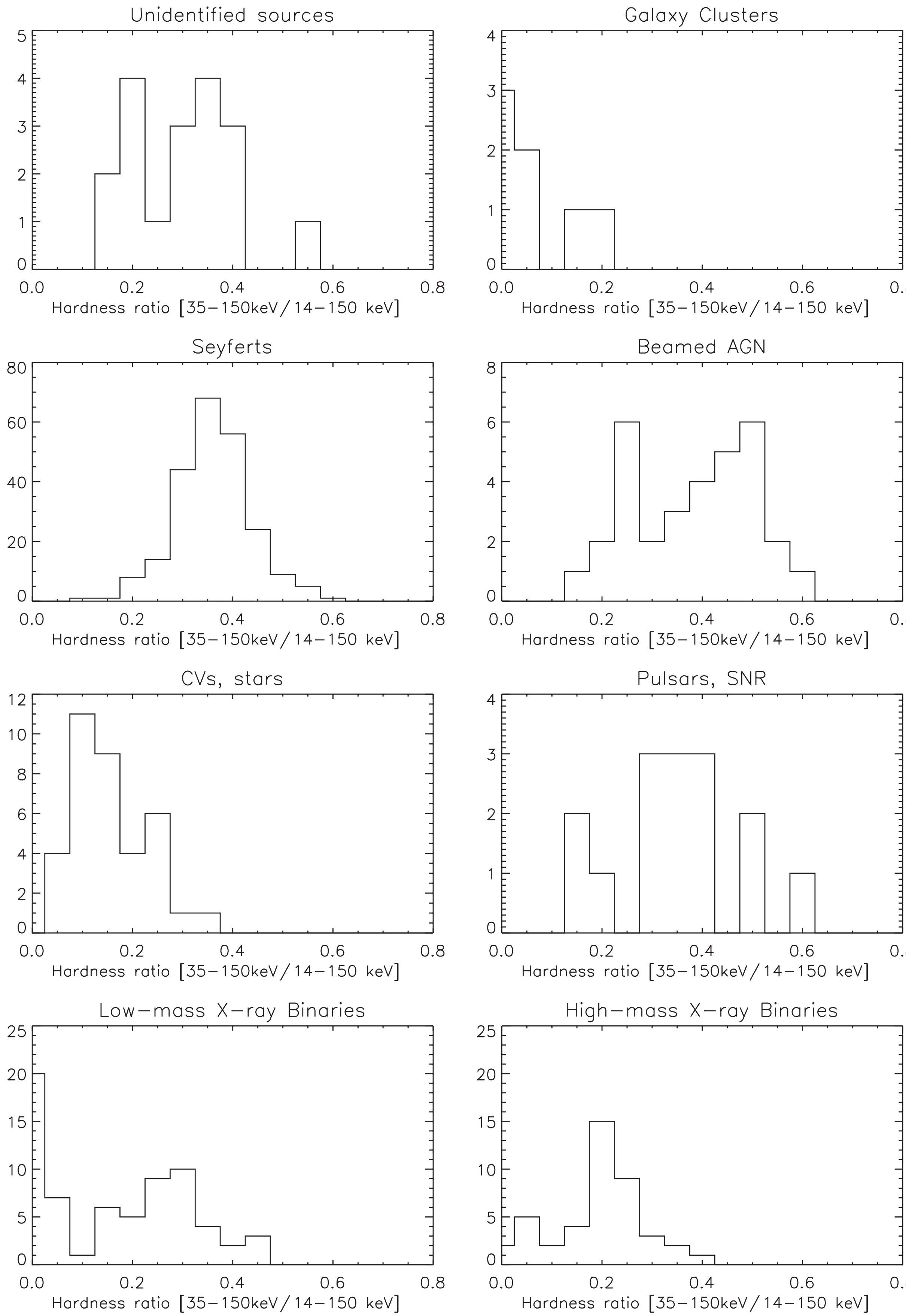

Figure 9. Hardness ratios of BAT 22-month sources by source class.

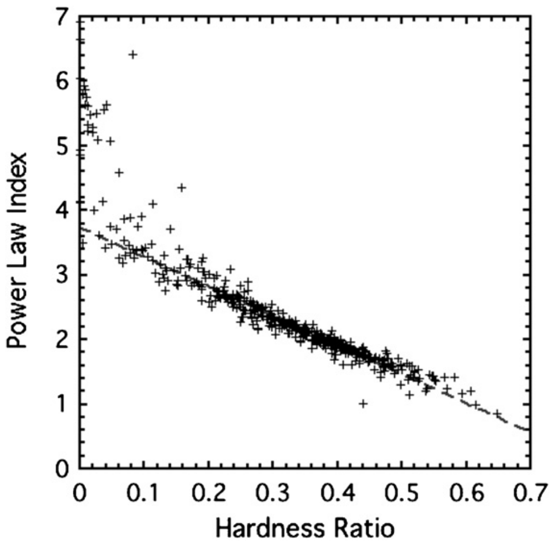

Figure 10. Correlation between power-law index and hardness ratio for the BAT survey sources.

Most of the sources in the 9-month catalog also appear here in the 22-month catalog; however, variability in the sources has caused 11 sources to drop out of the 22-month list that were in the 9-month catalog.

5.1. New Sources

During the survey BAT has detected a number of new sources that are transients or other Galactic objects not previously reported as hard X-ray sources. Some of these have been reported in Astronomer's Telegrams or elsewhere, others appear for the first time in this compilation. For convenience these are summarized in Table 2.

In Table 3, we note other sources that are detected in this survey and where XRT follow-up has provided additional information, but where a unique optical, IR, or radio counterpart is still lacking, or where there is only a BAT detection. Some of these are almost certainly Galactic objects as may be judged from their proximity to the Galactic plane.

Table 4 lists the new AGN discovered in the 22-month *Swift*-BAT survey. Table 4 lists those objects discovered with BAT whose AGN nature could be confirmed with an optical spectrum. In Column 3 of the table we list the source of the optical data, and Columns 4 and 5 list our own typing of the spectrum and the redshift. The optical spectra are mostly obtained from data in the public domain such as Sloan Digital Sky Survey (SDSS) or 6df, but in a few cases we have obtained data from our own observations taken at the 2.1 m telescope on Kitt Peak.

5.2. Extragalactic Sources

Most of the extragalactic identifications are with relatively nearby Seyfert galaxies and many of the remainder are with beamed AGN (blazars, BL Lac, FSRQ, etc.) sources at much higher z.

Figure 11 shows some typical BAT source host galaxy images from the Palomar digital sky survey. The field of view is 2 arcmin across for each subimage. The figure was produced by dividing the hardness-luminosity plane into 70 bins and randomly choosing a BAT source from that category to display. Of note are the high fraction of spiral galaxy hosts (as opposed to ellipticals) and the high number of interacting galaxies.

Table 2
New High Energy Sources in the 22-month Catalog that are Galactic, or Probably Galactic, and were First Detected as Hard X-ray Sources by *Swift*-BAT

Source	First Reported	Notes
SWIFT J0026.1+0508	Here	Of several sources in an XRT follow-up observation, only one is hard and it is taken to be the counterpart. It could be a CV.
SWIFT J0732.5−1331	ATel 697	CV of subtype DQ Her. ATels 757, 760, 763.
SWIFT J1010.1−5747	ATel 684	= CD−57 3057. ATel 669 gives XRT position for BAT source SWIFT J1011.1−5748 = IGRJ 10109−5746 associated with Symbiotic star CD-57 3057 (ATel 715).
SWIFT J1515.2+1223	Here	In a 7400 s XRT follow-up, only one source is detected in the hard band at $(\alpha, \delta) = (15\,14\,47, +12\,22\,44)$. No known counterparts at this position.
SWIFT J1546.3+6928	Here	The BAT source is confused. There are TWO hard (>3 keV) sources in the XRT image, 1RXS J154534.5+692925 AND 2MASS J15462424+6929102. There are some indications that the ROSAT source is extended, perhaps an interacting pair (making a possible third source). The 2MASS object is extended and clearly a galaxy.
SWIFT J1559.6+2554	ATel 668/9	= T CrB. The Swift source is identified with this symbiotic star in XRT follow-up.
SWIFT J1626.9−5156	ATel 678	Peculiar (HMXB?) transient. 15.37 s pulsations. Optical counterpart 2MASS16263652−5156305. Short (100–1000s) flares (Reig et al. 2008).
SWIFT J1753.5−0130	ATel 546	Short period (3.2 hr; ATel 1130) BH LMXB transient observed with many other instruments following BAT detection.
SWIFT J1907.3−2050	Here	= V1082 Sgr. XRT follow-up shows a strong hard source coincident with the pulsating variable star. Steiner et al. (1988) have found that this star in its hard state has properties similar to a CV of subtype DQ Her. Thorstensen et al. (2009) has determined an orbital period of 20.821 hr for this object which classifies it as a long period CV.
SWIFT J1922.7−1717	ATel 669	Transient observed with RXTE and Integral after BAT detection (Falanga et al. 2006)
SWIFT J1942.8+3220	Here	= V2491 Cyg. We find a weak hard X-ray source whose position is consistent with V2491 Cyg in data taken before its eruption as Nova Cyg 2008b. (see also Ibarra et al. (2009), ATel 1478)
SWIFT J2037.2+4151	ATel 853	Transient; later seen with Integral (ATel 967)
SWIFT J231930.4+261517	ATel 1309	XRT data show that this source is the same as 1RXS J231930.9+261525, reported and identified as a CV of subtype AM Her in ATel 1309. Mkn 322 and UGC 12515 may also contribute to the BAT counts
SWIFT J2327.6+0629	Here	There is no clear source in the XRT field.

Table 3
Unidentified New Sources

Source	l[a] (°)	b(°)	Notes
SWIFT J0826.2−7033	284.21	−18.09	= 1ES 0826−703, 1RXS J082623.5−703142. The 4″.1 radius XRT position is 1″.2 from T Tau star 2MASS J08262350−7031431.
SWIFT J1515.2+1223	16.44	+53.28	Nearest XRT source is a weak one 7′.8 away, just outside the 5′ radius BAT error circle.
SWIFT J1546.3+6928	104.27	40.74	Two hard XRT sources lie within the BAT error circle. One is associated with 1RXS J154534.5+692925, about which nothing is known, the other is coincident with the extended source 2MASX J15462424+6929102, which is identified with LEDA 2730634, a side-on spiral galaxy.
SWIFT J1706.6−6146	328.72	−12.40	= IGRJ17062−6143. Bright XRT counterpart gives precise position but no apparent optical/IR/Radio counterpart.
SWIFT J1709.8−3627	349.55	2.07	= IGR J17098−3628. IGR J17091−3624 is only 8′.5 away. XRT provides positions for both (ATel 1140). The BAT position corresponds to IGR J17098−3628, but the XRT error circle contains a complex of IR sources and a radio source and it is not clear which are counterparts.

Notes. These sources have new information but no firm identification with an optical/IR/Radio object.
[a] Galactic coordinates are given as an indication of whether the sources is likely to be Galactic.

Table 4
New AGN Detected in the *Swift*-BAT 22-month Survey with Optical Spectroscopic Confirmation

BAT Name	Host Galaxy	Optical Spectrum[a]	Galaxy Type	Redshift
SWIFT J0100.9−4750	2MASX J01003490−4752033	6df	Sy1.8	
SWIFT J0623.8−3215	ESO 426- G 002	6df	Sy2	
SWIFT J0923.9−3143	2MASX J09235371−3141305	6df	Sy1.8	
SWIFT J1513.8−8125	2MASX J15144217−8123377	6df	Sy1.8	
SWIFT J0249.1+2627	2MASX J02485937+2630391	KP	XBONG[b]	0.058
SWIFT J0353.7+3711	2MASX J03534246+3714077	KP	Sy2	0.01828
SWIFT J0543.9−2749	MCG −05-14-012	KP	XBONG	0.0099
SWIFT J0544.4+5909	2MASX J05442257+5907361	KP	Sy1.9	0.06597
SWIFT J1246.6+5435	NGC 4686	KP	XBONG	0.0167
SWIFT J1621.2+8104	CGCG 367−009	KP	Sy2	0.0274
SWIFT J1830.8+0928	2MASX J18305065+0928414	KP	Sy2	0.019
SWIFT J2118.9+3336	2MASX J21192912+3332566	KP	Sy1	0.0507
SWIFT J2341.8+3033	UGC 12741	KP	Sy2	0.0174

Notes.
[a] The optical spectra sources are as follows: 6df = Six degree field galaxy survey, SDSS, Sloan Digital Sky Survey; KP, 2.1 m at Kitt Peak.
[b] XBONG: (hard) X-ray Bright, Optically Normal Galaxy.

The 234 sources that have an identification with a well-established Seyfert galaxy more than double the number in any previous hard X-ray survey. The distribution of column densities, spectral indices, and luminosities for the survey sources will be presented in a separate paper. As elsewhere in this paper, we emphasize that this catalog is based on mean flux levels over the entire 22 month period. The detections of sources with significant temporal variability over the survey period and the implications of such variability will be discussed elsewhere. Figure 12 shows a histogram of the redshifts of all the AGNs found in the 22-month catalog. The distribution of the Seyfert galaxy redshifts from the 22-month survey (left panel of Figure 12) is highly biased towards low redshifts ($z \sim 0.03$) with a tail extending out to $z \sim 0.1$ and a few more distant objects out to $z \sim 0.3$. The right panel of Figure 12 shows the redshift distribution of the beamed AGN. This distribution is quite different from the Seyfert galaxies in the left panel, with redshifts that extend to $z \sim 4$ and with no objects at $z < 0.033$. Since we have no selection biases with respect to these beamed AGN (as opposed to optical searches for blazars) these different redshift distributions are a fundamental property of these classes and are directly related to their luminosity functions and evolution (Ajello et al. 2009b).

Figure 13 is a histogram of the luminosities of the Seyfert galaxies detected in the BAT 22-month survey. The luminosity distribution of the Seyfert galaxies continues to show a difference between the type Is and type IIs as noted in Winter et al. (2008). This indicates that the true luminosity distribution is indeed different for these two classes, which is inconsistent with the unified model of AGN. A K-S test of these two luminosity distributions shows that they are drawn from the same parent distribution with a probability of only 0.30.

As in earlier hard X-ray surveys, the second most common category of extragalactic sources are beamed AGNs, which include types such as blazars, BL Lacs, FSRQs, etc. There are 32 objects in this category. The highest redshift is for QSO J0539−2839 at $z = 3.104$.

We have detected 10 clusters of galaxies at $>4.8\sigma$; Perseus, Coma, Ophiuchus, Cygnus A, Abell 2319, Abell 754, Abell 3266, Abell 2142, Abell 3571, and Triangulum Australis.

Table 5
Catalog of Sources in the 22-month *Swift*-BAT Survey

#	BAT Name[a]	R.A.[b]	Decl.	S/N	Counterpart Name	Other Name	Ctpt R.A.[c]	Ctpt Decl.	Flux[d]	Error	C[e]	Hrat[f]	Herr	Redshift[g]	Lum[h]	Type
1	SWIFT J0006.3+2011	1.570	20.177	7.05	MRK 0335		1.5813	20.2029	2.47	0.41		0.31	0.07	0.0258	43.57	Sy1.2
2	SWIFT J0010.4+1100	2.607	10.992	7.59	MRK 1501		2.6292	10.9749	4.10	0.55		0.40	0.05	0.0893	44.91	Sy1.2
3	SWIFT J0025.3+6821	6.322	68.351	5.76	2MASX J00253292+6821442		6.3870	68.3623	3.02	0.66		0.51	0.09	0.0120	42.99	Sy2
4	SWIFT J0026.1+0508	6.527	5.139	5.55	SWIFT J002615.1+050417		6.5631	5.0715	4.13	1.12		0.59	0.12	?		
5	SWIFT J0029.0+5918	7.244	59.296	24.30	V709 Cas	RX J0028.8+5917	7.2036	59.2894	8.91	0.39		0.25	0.02			CV/DQ Her
6	SWIFT J0036.0+5953	9.007	59.876	5.76	QSO B0033+595	1ES 0033+595	8.9694	59.8346	1.96	0.34		0.19	0.07	0.0860	44.56	BL Lac
7	SWIFT J0037.3+6122	9.337	61.363	6.45	BD +60 73	IGR J0370+6122	9.2902	61.3601	2.85	0.47		0.35	0.06			HMXB
8	SWIFT J0042.9−2332	10.706	−23.491	7.00	NGC 235A		10.7200	−23.5410	4.12	0.48		0.35	0.05	0.0222	43.67	Sy1
9	SWIFT J0048.8+3155	12.198	31.953	28.85	Mrk 348		12.1964	31.9570	13.66	0.56		0.42	0.02	0.0150	43.84	Sy2
10	SWIFT J0051.9+1724	12.964	17.394	7.36	MRK 1148		12.9783	17.4329	2.80	0.41		0.24	0.06	0.0640	44.44	Sy1
11	SWIFT J0052.0−7319	12.989	−73.312	11.40	RX J0052.1−7319	2E 0050.4−7335	13.0921	−73.3181	5.70	0.42		0.28	0.03			HMXB
12	SWIFT J0055.4+4612	13.852	46.208	6.52	1RXS J005528.0+461143		13.8671	46.1953	1.97	0.28		0.10	0.07			CV/DQ Her
13	SWIFT J0056.6+6043	14.161	60.718	24.03	Gamma Cas	4U 0054+60	14.1772	60.7167	7.08	0.26		0.08	0.02			Star/Be
14	SWIFT J0059.4+3150	14.957	31.821	9.50	Mrk 352		14.9720	31.8269	4.16	0.50		0.37	0.05	0.0149	43.31	Sy1
15	SWIFT J0100.9−4750	15.222	−47.833	6.44	ESO 195-IG 021 NED03		15.1457	−47.8676	2.08	0.45		0.35	0.08	0.0483	44.06	Sy1.8
16	SWIFT J0108.7+1320	17.173	13.340	8.60	3C 033		17.2203	13.3372	4.06	0.52		0.38	0.05	0.0597	44.54	Sy2
17	SWIFT J0113.8−1454	18.448	−14.899	5.49	MRK 1152		18.4587	−14.8456	2.50	0.45		0.28	0.07	0.0527	44.22	Sy1.5
18	SWIFT J0117.1−7327	19.273	−73.446	111.96	SMC X-1	4U 0115−73	19.2714	−73.4433	38.20	0.29		0.08	0.00			HMXB/NS
19	SWIFT J0118.0+6518	19.508	65.296	51.69	V662 Cas	4U 0114+65	19.5112	65.2916	17.14	0.37		0.22	0.01			HMXB/NS
20	SWIFT J0122.9+3420	20.726	34.341	5.98	SHBL J012308.7+342049	2E 0120.3+3404	20.7860	34.3469	2.12	0.43		0.28	0.08	0.2720	45.69	BL Lac
21	SWIFT J0123.9−5846	20.965	−58.779	12.38	Fairall 9		20.9408	−58.8057	5.07	0.45		0.33	0.03	0.0470	44.42	Sy1
22	SWIFT J0123.8−3504	20.973	−35.063	11.37	NGC 526A		20.9766	−35.0654	5.96	0.51		0.39	0.03	0.0191	43.69	Sy1.5
23	SWIFT J0124.4+3348	21.100	33.805	4.80	NGC 0513		21.1119	33.7995	2.06	0.43		0.25	0.09	0.0195	43.25	Sy2
24	SWIFT J0134.1−3625	23.516	−36.458	6.58	NGC 0612		23.4906	−36.4933	5.35	0.61		0.50	0.05	0.0298	44.04	Radio galaxy
25	SWIFT J0138.6−4001	24.717	−39.991	12.97	ESO 297−018		24.6548	−40.0114	7.37	0.54		0.45	0.03	0.0252	44.03	Sy2
26	SWIFT J0146.4+6143	26.588	61.725	13.28	PSR J0146+61		26.5934	61.7509	12.29	0.89		0.65	0.04			AXP
27	SWIFT J0152.8−0329	28.198	−3.462	5.67	MCG −01-05-047		28.2042	−3.4468	2.78	0.46		0.28	0.07	0.0172	43.27	Sy2
28	SWIFT J0201.0−0648	30.263	−6.812	18.20	NGC 788		30.2769	−6.8155	9.33	0.57		0.46	0.03	0.0136	43.59	Sy2
29	SWIFT J0206.2−0019	31.564	−0.307	5.55	Mrk 1018		31.5666	−0.2914	3.61	0.64		0.47	0.08	0.0424	44.18	Sy1.5
30	SWIFT J0209.7+5226	32.394	52.446	11.75	LEDA 138501		32.3929	52.4425	5.48	0.53		0.37	0.04	0.0492	44.50	Sy1
31	SWIFT J0216.3+5128	34.061	51.401	6.95	2MASX J02162987+5126246		34.1243	51.4402	2.93	0.48		0.34	0.07	?		likely Sy2
32	SWIFT J0218.0+7348	34.193	73.817	6.99	[HB89] 0212+735		34.3784	73.8257	3.33	0.57		0.43	0.06	2.3670	48.16	BL Lac
33	SWIFT J0225.0+1848	36.249	18.806	5.42	RBS 0315		36.2695	18.7802	2.71	0.60		0.42	0.08	2.6900	48.21	BL Lac
34	SWIFT J0228.1+3118	37.061	31.323	14.34	NGC 931		37.0603	31.3117	6.56	0.50		0.30	0.03	0.0167	43.61	Sy1.5
35	SWIFT J0231.6−3645	37.892	−36.737	6.09	IC 1816		37.9625	−36.6721	2.58	0.48		0.39	0.07	0.0170	43.22	Sy1.8
36	SWIFT J0234.1+3233	38.512	32.555	5.69	NGC 0973		38.5838	32.5056	3.09	0.58		0.42	0.08	0.0162	43.26	Sy2
37	SWIFT J0234.6−0848	38.663	−8.760	7.70	NGC 985		38.6574	−8.7876	3.45	0.46		0.33	0.05	0.0430	44.17	Sy1
38	SWIFT J0235.3−2934	38.877	−29.593	7.91	ESO 416-G002		38.8061	−29.6047	3.40	0.60		0.46	0.06	0.0592	44.46	Sy1.9
39	SWIFT J0238.2−5213	39.584	−52.191	10.17	ESO 198−024		39.5821	−52.1923	4.98	0.50		0.41	0.04	0.0455	44.38	Sy1
40	SWIFT J0240.5+6117	40.116	61.286	7.04	LS I +61 303	V615 Cas	40.1319	61.2293	3.09	0.52		0.35	0.06			HMXB
41	SWIFT J0241.3−0815	40.331	−8.245	7.08	NGC 1052		40.2700	−8.2558	3.75	0.67		0.43	0.07	0.0050	42.32	Sy2
42	SWIFT J0242.8−0002	40.710	−0.033	7.07	NGC 1068		40.6696	−0.0133	3.72	0.53		0.37	0.06	0.0038	42.07	Sy2
43	SWIFT J0244.8+6227	41.275	62.450	16.54	[HB89] 0241+622		41.2404	62.4685	8.59	0.57		0.39	0.03	0.0440	44.59	Sy1

Table 5
(Continued)

#	BAT Name[a]	R.A.[b]	Decl.	S/N	Counterpart Name	Other Name	Ctpt R.A.[c]	Ctpt Decl.	Flux[d]	Error	C[e]	Hrat[f]	Herr	Redshift[g]	Lum[h]	Type
44	SWIFT J0249.1+2627	42.171	26.424	6.00	2MASX J02485937+2630391		42.2472	26.5109	3.91	0.82		0.47	0.08	0.0579	44.50	Sy2
45	SWIFT J0251.3+5441	42.705	54.687	5.18	2MFGC 02280		42.6775	54.7049	3.30	0.57		0.43	0.08	0.0152	43.23	Galaxy
46	SWIFT J0252.7−0822	43.176	−8.481	5.10	MCG −02-08-014		43.0975	−8.5104	2.43	0.47		0.28	0.08	0.0168	43.19	Sy2, hidden
47	SWIFT J0255.2−0011	43.798	−0.197	17.53	NGC 1142		43.8008	−0.1836	10.13	0.60		0.43	0.02	0.0289	44.29	Sy2
48	SWIFT J0256.2+1926	44.049	19.426	7.11	XY Ari	2E 0253.3+1914	44.0375	19.4414	3.12	0.46		0.28	0.06			CV/DQ Her
49	SWIFT J0256.4−3212	44.096	−32.212	7.29	ESO 417- G 006		44.0898	−32.1856	3.06	0.46		0.36	0.06	0.0163	43.26	Sy2
50	SWIFT J0304.1−0108	46.011	−1.125	7.47	NGC 1194	LEDA 11537	45.9546	−1.1037	3.64	0.60		0.43	0.07	0.0136	43.18	Sy1
51	SWIFT J0311.1+3240	47.785	32.662	4.89	2MASX J03104435+3239296		47.6850	32.6580	1.85	0.44		0.28	0.10	0.1270	44.89	Sy
52	SWIFT J0311.5−2045	47.841	−20.744	5.28	RX J0311.3−2046		47.8284	−20.7717	2.98	0.60		0.50	0.08	0.0660	44.50	Sy1.5
53	SWIFT J0318.7+6828	49.664	68.443	4.85	2MASX J03181899+6829322		49.5791	68.4921	3.16	0.58		0.40	0.07	0.0901	44.81	Sy1.9
54	SWIFT J0319.7+4132	49.950	41.519	24.24	NGC 1275		49.9507	41.5117	6.85	0.28		0.14	0.02	0.0176	43.68	Sy2
55	SWIFT J0324.9+4044	51.191	40.745	6.29	UGC 02724		51.3565	40.7731	2.86	0.58		0.38	0.08	0.0477	44.19	Sy2 binary AGN
56	SWIFT J0325.0+3412	51.238	34.202	5.91	B2 0321+33 NED02		51.1715	34.1794	4.83	0.83		0.50	0.07	0.0610	44.64	Sy1
57	SWIFT J0328.4−2846	52.125	−28.777	5.15	PKS 0326−288		52.1522	−28.6989	3.25	0.73		0.54	0.09	0.1080	44.99	Sy1.9
58	SWIFT J0329.3−1320	52.337	−13.332	4.84	SWIFT J0329.3−1320		52.3347	−13.3966	2.09	0.63		0.43	0.09			
59	SWIFT J0331.2+4354	52.795	43.892	13.69	GK Per	3A 0327+438	52.7993	43.9047	4.83	0.35		0.18	0.04			CV/DQ Her
60	SWIFT J0333.6−3607	53.391	−36.144	20.10	NGC 1365		53.4016	−36.1404	7.19	0.44		0.35	0.02	0.0055	42.68	Sy1.8
61	SWIFT J0335.0+5311	53.743	53.176	312.24	BQ Cam	EXO 0331+530	53.7495	53.1732	90.31	0.27		0.08	0.00			HMXB/NS
62	SWIFT J0336.5+3219	54.117	32.312	6.55	4C 32.14		54.1255	32.3082	3.09	0.51		0.34	0.06	1.2580	47.45	QSO
63	SWIFT J0336.5−2509	54.179	−25.180	5.36	ESO 482−14	SWIFT J0336.8−2515	54.2632	−25.2492	2.25	0.56		0.42	0.08	0.0437	44.00	Sy2
64	SWIFT J0342.0−2115	55.508	−21.245	9.64	ESO 548-G081		55.5155	−21.2444	4.57	0.49		0.40	0.04	0.0145	43.33	Sy1
65	SWIFT J0349.2−1159	57.315	−11.950	7.28	QSO B0347−121	1ES 0347−12.1	57.3467	−11.9908	2.84	0.44		0.27	0.06	0.1800	45.41	BL Lac
66	SWIFT J0350.1−5019	57.559	−50.312	7.03	2MASX J03502377−5018354		57.5990	−50.3099	3.09	0.49		0.42	0.06	0.0365	43.98	SyX 6df
67	SWIFT J0353.4−6830	58.331	−68.494	5.24	PKS 0352−686		58.2396	−68.5214	1.65	0.37		0.26	0.08	0.0870	44.49	BL Lac
68	SWIFT J0353.7+3711	58.428	37.184	5.21	2MASX J03534246+3714077		58.4270	37.2350	1.72	0.45		0.27	0.09	0.0183	43.11	Sy2
69	SWIFT J0355.4+3103	58.846	31.046	106.34	X Per	4U 0352+309	58.8462	31.0458	60.13	0.58		0.36	0.00			HMXB/NS
70	SWIFT J0402.4−1807	60.604	−18.137	5.20	ESO 549- G 049		60.6070	−18.0480	2.65	0.61		0.57	0.11	0.0263	43.62	Sy2 LINER
71	SWIFT J0407.4+0339	61.852	3.729	6.92	3C 105		61.8186	3.7072	3.89	0.62		0.37	0.06	0.0890	44.89	Sy2
72	SWIFT J0414.8−0754	63.697	−7.914	5.58	IRAS 04124−0803		63.7195	−7.9278	2.52	0.48		0.31	0.07	0.0379	43.93	Sy1
73	SWIFT J0418.3+3800	64.582	38.038	25.59	3C 111.0		64.5887	38.0266	14.12	0.61		0.40	0.02	0.0485	44.89	Sy1
74	SWIFT J0422.7−5611	65.734	−56.222	5.26	ESO 157- G 023		65.6008	−56.2260	3.02	0.49		0.44	0.07	0.0435	44.13	Sy2
75	SWIFT J0426.2−5711	66.533	−57.178	5.04	1H 0419−577		66.5035	−57.2001	2.11	0.33		0.23	0.07	0.1040	44.77	Sy1
76	SWIFT J0431.5−6126	67.868	−61.440	5.10	ABELL 3266		67.7997	−61.4063	1.23	0.22		0.16	0.09	0.0589	44.01	Galaxy cluster
77	SWIFT J0433.0+0521	68.293	5.366	19.22	3C 120		68.2962	5.3543	11.89	0.63		0.39	0.02	0.0330	44.48	Sy1
78	SWIFT J0438.2−1048	69.552	−10.807	5.85	MCG −02-12-050		69.5591	−10.7959	2.11	0.40		0.23	0.08	0.0364	43.81	Sy1.2
79	SWIFT J0443.8+2855	70.952	28.924	4.88	UGC 03142		70.9450	28.9718	3.43	0.63		0.42	0.08	0.0217	43.56	Sy1
80	SWIFT J0444.1+2813	71.028	28.226	10.28	2MASX J04440903+2813003		71.0376	28.2168	7.02	0.69		0.44	0.04	0.0113	43.30	Sy2
81	SWIFT J0450.7−5813	72.738	−58.223	5.44	RBS 594		72.9335	−58.1835	3.17	0.60		0.48	0.08	0.0907	44.82	Sy1.5
82	SWIFT J0452.2+4933	72.985	49.508	13.24	1RXS J045205.0+493248		73.0208	49.5459	6.87	0.56		0.39	0.03	0.0290	44.12	Sy1
83	SWIFT J0453.4+0404	73.347	4.065	6.45	CGCG 420−015		73.3573	4.0616	4.08	0.68		0.47	0.08	0.0294	43.91	Sy2
84	SWIFT J0455.4−7533	73.857	−75.545	4.86	ESO 033- G 002		73.9957	−75.5412	2.61	0.45		0.33	0.07	0.0181	43.29	Sy2
85	SWIFT J0503.0+2302	75.738	23.021	6.14	LEDA 097068		75.7426	22.9977	3.41	0.63		0.35	0.07	0.0577	44.43	Sy1
86	SWIFT J0505.8−2351	76.445	−23.845	13.95	2MASX J05054575−2351139		76.4405	−23.8539	7.16	0.54		0.43	0.03	0.0350	44.31	Sy2 HII

Table 5
(Continued)

#	BAT Name[a]	R.A.[b]	Decl.	S/N	Counterpart Name	Other Name	Ctpt R.A.[c]	Ctpt Decl.	Flux[d]	error	C[e]	Hrat[f]	Herr	Redshift[g]	Lum[h]	Type
87	SWIFT J0510.7+1629	77.703	16.491	15.72	IRAS 05078+1626	4U 0517+17	77.6896	16.4989	9.34	0.68		0.38	0.03	0.0179	43.83	Sy1.5
88	SWIFT J0514.2−4004	78.539	−40.067	14.07	NGC 1851 XRB	4U 0513−40	78.5275	−40.0436	4.01	0.26		0.17	0.03			LMXB/NS
89	SWIFT J0516.2−0009	79.044	−0.159	14.12	Ark 120		79.0476	−0.1498	7.08	0.57		0.36	0.03	0.0323	44.23	Sy1
90	SWIFT J0501.9−3239	79.849	−32.686	13.78	ESO 362−18		79.8993	−32.6578	6.22	0.52		0.43	0.03	0.0125	43.33	Sy1.5
91	SWIFT J0519.5−4545	79.923	−45.768	8.82	PICTOR A		79.9570	−45.7790	3.78	0.46		0.38	0.04	0.0351	44.03	Sy1/LINER
92	SWIFT J0520.2−7156	80.052	−71.928	5.85	LMC X-2	4U 0520−72	80.1168	−71.9648	1.65	0.16		0.00	0.08			LMXB
93	SWIFT J0519.5−3140	80.737	−36.475	7.74	PKS 0521−36		80.7416	−36.4586	3.42	0.49		0.47	0.05	0.0553	44.40	BL Lac
94	SWIFT J0524.1−1210	81.072	−12.249	5.93	IRAS 05218−1212		81.0271	−12.1666	2.50	0.54		0.37	0.08	0.0490	44.15	Sy1
95	SWIFT J0529.2−3247	82.347	−32.834	18.98	TV Col	3A 0527−329	82.3560	−32.8179	5.11	0.29		0.19	0.02			CV/DQ Her
96	SWIFT J0532.8−6622	83.209	−66.369	77.12	RX J0531.2−6609	IGR J05319−6601	82.8054	−66.1181	4.99		A	0.20				HMXB/NS
97	"	"	"	"	LMC X-4	4U 0532−664	83.2075	−66.3705	31.64	0.34	B	0.15	0.00			HMXB/NS
98	SWIFT J0534.5+2201	83.632	22.017	3282.76	Crab Nebula/Pulsar		83.6332	22.0145	2386.15	0.66		0.35	0.00			PSR/PWN
99	SWIFT J0538.9+2619	84.733	26.324	132.18	V725 Tau	3A 0535+262	84.7274	26.3158	81.41	0.51		0.20	0.00			HMXB/NS
100	SWIFT J0539.1−6405	84.786	−64.083	7.08	LMC X-3	4U 0538−64	84.7342	−64.0823	3.11	0.48		0.32	0.06			HMXB/NS
101	SWIFT J0539.9−2839	84.933	−28.693	7.12	[HB89] 0537−286		84.9762	−28.6655	5.06	0.69		0.59	0.07	3.1040	48.63	Blazar
102	SWIFT J0539.7−6944	84.937	−69.741	9.22	LMC X-1	4U 0540−69	84.9113	−69.7433	3.98	0.39		0.25	0.04			HMXB/NS
103	SWIFT J0539.9−6921	84.987	−69.354	8.41	PSR B0540−69		85.0322	−69.3348	4.80	0.53		0.38	0.04			PSR
104	SWIFT J0542.8+6050	85.707	60.835	7.03	BY Cam	4U 0541+60	85.7038	60.8588	2.91	0.42		0.21	0.06			CV/AM Her
105	SWIFT J0543.3−4101	85.832	−41.014	6.08	TX Col	1H 0542−407	85.8343	−41.0320	1.80	0.26		0.13	0.07			CV/DQ Her
106	SWIFT J0543.9−2749	85.926	−27.687	4.90	MCG −05-14-012		85.8873	−27.6514	2.05	0.44		0.36	0.08	0.0099	42.65	Galaxy
107	SWIFT J0544.4+5909	86.084	59.162	5.23	2MASX J05442257+5907361		86.0941	59.1267	2.54	0.67		0.38	0.09	0.0660	44.43	Sy1.9
108	SWIFT J0550.7−3212	87.703	−32.257	9.05	PKS 0548−322		87.6699	−32.2716	3.28	0.43		0.33	0.05	0.0690	44.58	BL Lac
109	SWIFT J0552.2−0727	88.040	−7.456	54.89	NGC 2110		88.0474	−7.4562	35.01	0.70		0.43	0.01	0.0078	43.67	Sy2
110	SWIFT J0554.8+4625	88.729	46.423	16.32	MCG +08-11-011		88.7234	46.4393	9.64	0.61		0.37	0.02	0.0205	43.96	Sy1.5
111	SWIFT J0557.9−3822	89.511	−38.334	10.44	2MASX J05580206−3820043	4U 0557−38	89.5083	−38.3346	3.99	0.37		0.27	0.04	0.0339	44.02	Sy1
112	SWIFT J0558.1+5355	89.515	53.911	8.20	V405 Aur	RX J0558.0+5353	89.4970	53.8958	3.17	0.37		0.15	0.05			CV/DQ Her
113	SWIFT J0602.2+2829	90.550	28.479	7.89	IRAS 05589+2828		90.5446	28.4728	6.82	0.84		0.38	0.05	0.0330	44.23	Sy1
114	SWIFT J0601.9−8636	91.300	−86.613	6.41	ESO 005- G 004		91.4235	−86.6319	4.48	0.60		0.49	0.07	0.0062	42.59	Sy2
115	SWIFT J0615.8+7101	93.913	71.036	25.20	Mrk 3		93.9015	71.0375	15.65	0.61		0.47	0.02	0.0135	43.81	Sy2
116	SWIFT J0617.1+0908	94.280	9.137	87.32	V1055 Ori	4U 0614+091	94.2804	9.1369	51.72	0.62		0.30	0.00			LMXB/NS
117	SWIFT J0623.8−3215	95.961	−32.249	6.56	ESO 426- G 002		95.9434	−32.2166	2.72	0.45		0.40	0.07	0.0224	43.49	Sy2
118	SWIFT J0640.4−2554	100.044	−25.900	10.94	ESO 490-IG026		100.0487	−25.8954	4.29	0.45		0.31	0.04	0.0248	43.78	Sy1.2
119	SWIFT J0640.1−4328	100.340	−43.285	5.16	2MASX J06403799−4321211		100.1583	−43.3558	2.00	0.46		0.37	0.09	?		Galaxy
120	SWIFT J0641.3+3257	100.381	32.884	6.59	2MASX J06411806+3249313		100.3252	32.8254	4.76	0.93		0.46	0.07	0.0470	44.39	Sy2
121	SWIFT J0651.9+7426	103.092	74.434	15.85	Mrk 6		103.0511	74.4271	7.61	0.55		0.42	0.03	0.0188	43.78	Sy1.5
122	SWIFT J0656.0+4000	103.991	39.993	6.29	UGC 03601		103.9564	40.0002	4.38	0.67		0.40	0.06	0.0171	43.46	Sy1.5
123	SWIFT J0731.3+0958	112.834	9.959	5.80	BG CMi	3A 0729+103	112.8708	9.9396	2.15	0.40		0.17	0.07			CV/DQ Her
124	SWIFT J0732.5−1331	113.168	−13.527	9.29	SWIFT J073237.6−133109	SWIFT J0732.5−1331	113.1563	−13.5178	2.97	0.37		0.19	0.05			CV/DQ Her
125	SWIFT J0742.5+4948	115.607	49.826	10.57	Mrk 79		115.6367	49.8097	4.89	0.52		0.37	0.04	0.0222	43.74	Sy1.2
126	SWIFT J0746.3+2548	116.635	25.810	8.10	SDSS J074625.87+254902.2		116.6078	25.8173	7.79	1.01		0.61	0.06	2.9793	48.77	Blazar
127	SWIFT J0747.5+6057	116.889	60.961	5.05	MRK 10		116.8714	60.9335	3.12	0.54		0.46	0.07	0.0293	43.79	Sy1.2
128	SWIFT J0748.6−6745	117.151	−67.753	76.87	UY Vol	EXO 0748−676	117.1388	−67.7500	34.49	0.44		0.31	0.00			LMXB/NS
129	SWIFT J0750.9+1439	117.810	14.726	7.22	PQ Gem	RX J0751.2+1444	117.8225	14.7402	3.03	0.39		0.12	0.06			CV/DQ Her
130	SWIFT J0759.8−3844	119.970	−38.731	10.03	2MASS J07594181−3843560	IGR J07597−3842	119.9208	−38.7600	5.62	0.56		0.38	0.04	0.0400	44.32	Sy1.2

Table 5
(Continued)

#	BAT Name[a]	R.A.[b]	Decl.	S/N	Counterpart Name	Other Name	Ctpt R.A.[c]	Ctpt Decl.	Flux[d]	Error	C[e]	Hrat[f]	Herr	Redshift[g]	Lum[h]	Type
131	SWIFT J0800.1+2638	120.023	26.649	5.37	IC 0486		120.0874	26.6135	3.22	0.70		0.42	0.07	0.0269	43.73	Sy1
132	SWIFT J0800.5+2327	120.038	23.404	6.88	2MASX J07595347+2323241	CGCG 118−036	119.9728	23.3901	4.28	0.72		0.51	0.07	0.0292	43.92	Sy2
133	SWIFT J0804.2+0507	121.032	5.129	11.50	Phoenix Galaxy		121.0244	5.1138	5.34	0.57		0.35	0.04	0.0135	43.34	Sy2
134	SWIFT J0823.4−0457	125.769	−4.894	5.30	FAIRALL 0272		125.7546	−4.9349	4.02	0.71		0.57	0.08	0.0218	43.64	Sy2
135	SWIFT J0826.2−7033	126.595	−70.536	5.19	1RXS J082623.5−703142	1ES 0826−703	126.5979	−70.5283	2.08	0.36		0.22	0.08			SRC/X-ray
136	SWIFT J0835.3−4511	128.831	−45.187	29.44	Vela Pulsar	PSR B0833−45	128.8361	−45.1764	18.19	0.56		0.40	0.01			PSR
137	SWIFT J0838.5−3559	129.615	−35.979	5.19	FAIRALL 1146		129.6283	−35.9926	3.27	0.51		0.30	0.06	0.0316	43.87	Sy1.5
138	SWIFT J0838.5+4839	129.631	48.642	7.78	EI UMa	RX J0838.3+4838	129.5916	48.6338	3.21	0.36		0.23	0.05			CV/DQ Her
139	SWIFT J0839.6−1213	129.912	−12.221	6.00	3C 206		129.9609	−12.2428	2.87	0.51		0.37	0.07	0.1976	45.51	QSO
140	SWIFT J0841.4+7052	130.399	70.900	16.54	[HB89] 0836+710		130.3515	70.8951	8.48	0.57		0.48	0.03	2.1720	48.48	Blazar
141	SWIFT J0902.1−4033	135.528	−40.555	1074.22	VELA X-1	4U 0900−40	135.5286	−40.5547	393.20	0.37		0.14	0.00			HMXB/NS
142	SWIFT J0904.3+5538	136.076	55.588	5.51	2MASX J09043699+5536025		136.1540	55.6008	1.91	0.40		0.32	0.08	0.0370	43.78	Sy1
143	SWIFT J0908.9−0936	137.235	−9.594	6.11	ABELL 0754		137.2087	−9.6366	1.76	0.23		0.00	0.10	0.0542	44.09	Galaxy cluster
144	SWIFT J0911.2+4533	137.851	45.557	6.11	2MASX J09112999+4528060		137.8749	45.4683	1.81	0.44		0.30	0.08	0.0268	43.47	Sy2
145	SWIFT J0917.2−6221	139.116	−62.283	8.24	IRAS 09149−6206		139.0392	−62.3249	3.26	0.46		0.32	0.05	0.0573	44.41	Sy1
146	SWIFT J0918.5+1618	139.629	16.323	8.09	Mrk 704		139.6084	16.3053	3.63	0.51		0.35	0.05	0.0292	43.85	Sy1.5
147	SWIFT J0920.4−5512	140.108	−55.194	18.57	2MASS J09202647−5512244	4U 0919−54	140.1105	−55.2070	9.00	0.42		0.28	0.02			LMXB
148	SWIFT J0920.8−0805	140.198	−8.103	8.91	MCG −01-24-012		140.1927	−8.0561	4.58	0.51		0.33	0.05	0.0196	43.60	Sy2
149	SWIFT J0923.7+2255	140.945	22.906	10.19	MCG +04-22-042		140.9292	22.9090	4.46	0.59		0.39	0.05	0.0323	44.03	Sy1.2
150	SWIFT J0923.8−3143	140.952	−31.716	5.42	2MASX J09235371−3141305		140.9739	−31.6919	1.77	0.41		0.22	0.09	0.0422	43.87	Sy1.9
151	SWIFT J0925.0+5218	141.288	52.297	14.14	Mrk 110		141.3036	52.2863	6.15	0.47		0.39	0.03	0.0353	44.25	Sy1
152	SWIFT J0926.0+1243	141.498	12.708	5.12	MRK 0705		141.5137	12.7343	2.13	0.45		0.30	0.09	0.0291	43.62	Sy1.2
153	SWIFT J0945.6−1420	146.440	−14.316	8.95	NGC 2992		146.4252	−14.3264	4.82	0.63		0.41	0.05	0.0077	42.80	Sy2
154	SWIFT J0947.6+0724	146.899	7.401	4.87	3C 227		146.9380	7.4224	2.65	0.50		0.35	0.08	0.0858	44.69	Sy1 BLRG
155	SWIFT J0947.6−3057	146.915	−30.945	41.91	MCG −05-23-016		146.9173	−30.9489	20.77	0.56		0.35	0.01	0.0085	43.52	Sy2
156	SWIFT J0950.2+7316	147.556	73.262	4.80	RIXOS F305−011		147.8070	73.3100	1.47		AB	0.39		0.2510	45.45	AGN
157	"	"	"	"	VII Zw 292		147.4410	73.2400	1.74		AB	0.38		0.0581	44.15	NLRG
158	SWIFT J0959.5−2248	149.878	−22.833	17.16	NGC 3081		149.8731	−22.8263	10.24	0.67		0.42	0.03	0.0080	43.16	Sy2
159	SWIFT J1001.9+5539	150.468	55.649	7.40	NGC 3079		150.4908	55.6798	3.44	0.44		0.43	0.05	0.0037	42.02	Sy2
160	SWIFT J1009.9−5818	152.465	−58.294	17.65	GRO J1008−57		152.4417	−58.2917	7.49	0.40		0.21	0.02			HMXB
161	SWIFT J1009.3−4250	152.474	−42.789	5.33	ESO 263- G 013		152.4509	−42.8112	2.61	0.51		0.30	0.07	0.0333	43.82	Sy2
162	SWIFT J1010.1−5747	152.668	−57.819	5.16	CD-57 3057	IGR J10109−5746	152.7623	−57.8039	2.25	0.36		0.13	0.07			Symb/WD
163	SWIFT J1013.5−3601	153.317	−36.016	5.23	ESO 374- G 044		153.3330	−35.9827	2.82	0.60		0.39	0.08	0.0284	43.72	Sy2
164	SWIFT J1023.5+1952	155.867	19.872	29.54	NGC 3227		155.8774	19.8651	14.13	0.50		0.38	0.01	0.0039	42.67	Sy1.5
165	SWIFT J1031.7−3451	157.951	−34.864	16.57	NGC 3281		157.9670	−34.8537	9.01	0.66		0.43	0.03	0.0107	43.36	Sy2
166	SWIFT J1038.8−4942	159.735	−49.803	5.98	2MASX J10384520−4946531		159.6883	−49.7816	4.89	0.76		0.55	0.07	0.0600	44.63	Sy1
167	SWIFT J1040.7−4619	160.054	−46.457	6.21	LEDA 093974		160.0939	−46.4238	3.68	0.65		0.39	0.07	0.0239	43.68	Sy2
168	SWIFT J1049.4+2258	162.375	22.997	7.10	Mrk 417		162.3789	22.9644	3.74	0.51		0.46	0.06	0.0328	43.97	Sy2
169	SWIFT J1052.8+1043	163.166	10.718	5.32	2MASX J10523297+1036205		163.1370	10.6060	2.60	0.61		0.51	0.09	0.0878	44.70	Sy1
170	SWIFT J1104.4+3812	166.110	38.210	63.14	Mrk 421		166.1138	38.2088	19.19	0.31		0.24	0.01	0.0300	44.60	BL Lac
171	SWIFT J1106.5+7234	166.649	72.573	30.47	NGC 3516		166.6979	72.5686	12.54	0.45		0.42	0.01	0.0088	43.34	Sy1.5
172	SWIFT J1121.2−6037	170.312	−60.624	249.54	Cen X-3	V779 Cen	170.3158	−60.6230	88.94	0.27		0.04	0.00			HMXB/NS
173	SWIFT J1127.5+1906	171.848	19.193	5.16	2MASX J11271632+1909198	1RXS J112716.6+190914	171.8178	19.1556	3.45	0.67		0.49	0.07	0.1055	44.99	Sy1.8
174	SWIFT J1130.2−1446	172.560	−14.773	6.66	PKS 1127−14		172.5294	−14.8243	4.70	0.88		0.52	0.07	1.1840	47.57	Blazar

Table 5
(Continued)

#	BAT Name[a]	R.A.[b]	Decl.	S/N	Counterpart Name	Other Name	Ctpt R.A.[c]	Ctpt Decl.	Flux[d]	Error	C[e]	Hrat[f]	Herr	Redshift[g]	Lum[h]	Type
175	SWIFT J1131.2−6257	172.788	−62.951	14.14	IGR J11305−6256		172.6417	−62.9300	5.44	0.44		0.23	0.03			HMXB
176	SWIFT J1132.9+5258	173.230	52.965	5.64	UGC 06527 NED03		173.1678	52.9504	2.68		AB	0.57		0.0278	43.68	Sy2
177	"	"	"	"	NGC 3718		173.1452	53.0679	2.69		AB	0.61		0.0033	41.81	Sy1 LINER
178	SWIFT J1136.7+6738	174.178	67.640	5.07	2MASX J11363009+6737042		174.1253	67.6179	1.61	0.37		0.27	0.09	0.1342	44.89	BL Lac
179	SWIFT J1139.0−3743	174.768	−37.730	34.57	NGC 3783		174.7572	−37.7386	19.45	0.66		0.38	0.01	0.0097	43.61	Sy1
180	SWIFT J1142.7+7149	175.789	71.721	6.96	DO Dra	YY Dra	175.9098	71.6890	1.74	0.24		0.13	0.07			CV/DQ Her
181	SWIFT J1144.2−6106	176.056	−61.092	11.86	IGR J11435−6109	1RXS J114358.1−610736 ?	175.9667	−61.1500	5.06	0.44		0.21	0.04			HMXB/NS
182	SWIFT J1143.7+7942	176.066	79.680	10.84	UGC 06728		176.3168	79.6815	2.95	0.37		0.32	0.05	0.0065	42.44	Sy1.2
183	SWIFT J1145.6−1819	176.412	−18.423	9.28	2MASX J11454045−1827149		176.4186	−18.4543	6.38	0.74		0.44	0.05	0.0329	44.20	Sy1
184	SWIFT J1147.5−6157	176.872	−61.958	73.37	1E 1145.1−6141		176.8692	−61.9539	30.96	0.44		0.23	0.01			HMXB/NS
185	SWIFT J1157.7+5528	179.417	55.473	6.32	NGC 3998		179.4839	55.4536	3.03	0.48		0.51	0.07	0.0035	41.91	Sy1 LINER
186	SWIFT J1200.8+0650	180.234	6.816	5.40	2MASX J12005792+0648226	CGCG 041−020	180.2413	6.8064	2.45	0.48		0.32	0.08	0.0360	43.87	Sy2
187	SWIFT J1200.2−5350	180.701	−53.852	8.04	LEDA 38038		180.6985	−53.8355	4.34	0.61		0.35	0.05	0.0280	43.89	Sy2
188	SWIFT J1203.0+4433	180.801	44.523	11.92	NGC 4051		180.7901	44.5313	4.34	0.35		0.31	0.03	0.0023	41.71	Sy1.5
189	SWIFT J1204.5+2019	181.109	20.281	5.98	ARK 347		181.1237	20.3162	3.85	0.58		0.45	0.06	0.0224	43.64	Sy2
190	SWIFT J1206.2+5243	181.607	52.679	6.96	NGC 4102		181.5963	52.7109	2.58	0.38		0.37	0.06	0.0028	41.66	LINER
191	SWIFT J1209.5+4702	182.337	47.019	5.29	MRK 0198		182.3088	47.0583	2.15	0.42		0.34	0.07	0.0242	43.46	Sy2
192	SWIFT J1209.4+4340	182.359	43.681	9.21	NGC 4138		182.3741	43.6853	3.69	0.45		0.43	0.05	0.0030	41.85	Sy1.9
193	SWIFT J1210.5+3924	182.636	39.406	121.30	NGC 4151		182.6357	39.4057	62.23	0.46		0.42	0.00	0.0033	43.18	Sy1.5
194	SWIFT J1213.2−6458	183.317	−64.929	6.22	SWIFT J121314.7−645231	4U 1210−64	183.3208	−64.8800	2.06	0.36		0.19	0.07			HMXB/NS
195	SWIFT J1217.3+0710	184.335	7.169	5.40	NGC 4235		184.2912	7.1916	2.40	0.55		0.39	0.08	0.0080	42.54	Sy1
196	SWIFT J1218.5+2952	184.621	29.814	7.67	Mrk 766		184.6105	29.8129	2.42	0.29		0.19	0.05	0.0129	42.96	Sy1.5
197	SWIFT J1219.4+4720	184.876	47.346	4.83	M106		184.7396	47.3040	2.80	0.63		0.51	0.09	0.0015	41.14	Sy1.9 LINER
198	SWIFT J1222.4+7519	185.595	75.314	7.02	MRK 0205		185.4333	75.3107	2.37	0.43		0.37	0.07	0.0708	44.46	BL Lac Sy1
199	SWIFT J1223.7+0238	185.853	2.638	5.31	MRK 0050		185.8506	2.6791	3.53	0.64		0.47	0.07	0.0234	43.64	Sy1
200	SWIFT J1202.5+3332	186.427	33.462	5.60	NGC 4395		186.4538	33.5468	3.12	0.41		0.36	0.05	0.0011	40.89	Sy1.9
201	SWIFT J1225.8+1240	186.443	12.664	51.62	NGC 4388		186.4448	12.6621	34.64	0.52		0.43	0.01	0.0084	43.74	Sy2
202	SWIFT J1226.6−6246	186.659	−62.769	675.04	GX 301−2		186.6567	−62.7706	261.13	0.36		0.06	0.00			LMXB/NS
203	SWIFT J1227.7−4854	186.919	−48.897	5.26	1RXS J122758.8−485343		186.9954	−48.8956	3.17	0.60		0.31	0.07			CV
204	SWIFT J1229.1+0202	187.278	2.048	68.66	3C 273		187.2779	2.0524	38.35	0.60		0.44	0.01	0.1583	46.42	Blazar
205	SWIFT J1234.7−6433	188.704	−64.576	15.01	RT Cru		188.7239	−64.5656	7.19	0.49		0.28	0.03			Symb/WD
206	SWIFT J1235.6−3954	188.893	−39.903	35.96	NGC 4507		188.9026	−39.9093	22.51	0.68		0.40	0.01	0.0118	43.85	Sy2
207	SWIFT J1238.9−2720	189.732	−27.313	22.02	ESO 506-G027		189.7275	−27.3078	13.75	0.72		0.44	0.02	0.0250	44.29	Sy2
208	SWIFT J1239.3−1611	189.785	−16.206	10.85	LEDA 170194	IGR J12392−1612	189.7763	−16.1799	6.87	0.76		0.45	0.04	0.0367	44.33	Sy2
209	SWIFT J1239.6−0519	189.904	−5.349	19.64	NGC 4593		189.9143	−5.3443	9.79	0.62		0.41	0.02	0.0090	43.25	Sy1
210	SWIFT J1240.9−3331	190.244	−33.548	5.38	ESO 381- G 007		190.1956	−33.5700	3.96	0.78		0.48	0.09	0.0550	44.46	Sy1.5
211	SWIFT J1241.6−5748	190.487	−57.828	5.07	WKK 1263		190.3570	−57.8340	4.03	0.78		0.58	0.10	0.0244	43.74	Sy1.5
212	SWIFT J1246.6+5435	191.724	54.550	7.22	NGC 4686		191.6661	54.5342	3.08	0.45		0.42	0.06	0.0167	43.29	Galaxy, XBONG
213	SWIFT J1249.6−5906	192.412	−59.100	21.74	4U 1246−58	1A 1246−588	192.4140	−59.0874	9.91	0.50		0.28	0.02			LMXB
214	SWIFT J1252.2−2917	193.057	−29.290	6.73	EX Hya		193.1017	−29.2491	2.54	0.35		0.15	0.07			CV/DQ Her
215	SWIFT J1256.2−0551	194.088	−5.812	6.91	3C 279		194.0465	−5.7893	4.97	0.74		0.55	0.07	0.5362	46.75	Blazar
216	SWIFT J1257.7−6918	194.433	−69.294	18.93	4U 1254−690		194.4048	−69.2886	5.80	0.23		0.05	0.02			LMXB/NS
217	SWIFT J1259.8+2757	194.943	27.952	8.29	Coma Cluster		194.9531	27.9807	3.59	0.19		0.02	0.03	0.0231	43.64	Galaxy cluster
218	SWIFT J1301.0−6139	195.257	−61.645	5.71	GX 304−1		195.3217	−61.6019	2.45	0.52		0.25	0.09			HMXB

Table 5
(Continued)

#	BAT Name[a]	R.A.[b]	Decl.	S/N	Counterpart Name	Other Name	Ctpt R.A.[c]	Ctpt Decl.	Flux[d]	Error	C[e]	Hrat[f]	Herr	Redshift[g]	Lum[h]	Type
219	SWIFT J1302.3−6359	195.571	−63.979	8.81	IGR J13020−6359		195.4983	−63.9683	3.99	0.42		0.22	0.04			PSR
220	SWIFT J1303.8+5345	196.032	53.772	8.86	SBS 1301+540		195.9978	53.7917	4.02	0.43		0.41	0.04	0.0299	43.92	Sy1
221	SWIFT J1305.4−4928	196.360	−49.464	42.73	NGC 4945		196.3645	−49.4682	32.98	0.77		0.50	0.01	0.0019	42.41	Sy2
222	SWIFT J1306.4−4025	196.672	−40.428	7.96	ESO 323−077		196.6089	−40.4146	4.70	0.66		0.35	0.05	0.0150	43.38	Sy1.2
223	SWIFT J1309.2+1139	197.286	11.658	13.08	NGC 4992		197.2733	11.6341	6.16	0.52		0.44	0.03	0.0251	43.95	Sy2 XBONG
224	SWIFT J1312.1−5631	197.969	−56.452	5.12	2MASX J13103701−5626551	SWIFT J1311.7−5629	197.6540	−56.4490	1.96	0.71		0.46	0.13	?		Galaxy
225	SWIFT J1322.2−1641	200.623	−16.723	6.31	MCG −03-34-064		200.6019	−16.7286	3.15	0.45		0.25	0.06	0.0165	43.29	Sy1.8
226	SWIFT J1325.4−4301	201.365	−43.022	138.27	Cen A		201.3651	−43.0191	92.62	0.71		0.42	0.00	0.0018	42.83	Sy2
227	SWIFT J1326.5−6208	201.636	−62.135	48.17	4U 1323−619		201.6504	−62.1361	24.60	0.53		0.29	0.01			LMXB/NS
228	SWIFT J1335.8−3416	203.973	−34.297	13.03	MCG −06-30-015		203.9741	−34.2956	7.82	0.57		0.32	0.03	0.0077	43.02	Sy1.2
229	SWIFT J1338.2+0433	204.561	4.557	14.38	NGC 5252		204.5665	4.5426	8.18	0.59		0.45	0.03	0.0230	43.99	Sy1.9
230	SWIFT J1347.4−6033	206.876	−60.605	14.51	4U 1344−60		206.9000	−60.6178	9.59	0.66		0.41	0.03	0.0129	43.55	Sy1.5
231	SWIFT J1349.3−3018	207.330	−30.312	56.95	IC 4329A		207.3303	−30.3094	33.08	0.62		0.37	0.01	0.0160	44.28	Sy1.2
232	SWIFT J1349.7+0209	207.425	2.153	6.29	UM 614		207.4701	2.0791	2.24	0.47		0.34	0.08	0.0327	43.74	Sy1
233	SWIFT J1352.8+6917	208.267	69.314	15.04	Mrk 279		208.2644	69.3082	5.30	0.38		0.35	0.03	0.0304	44.05	Sy1.5
234	SWIFT J1356.2+3832	209.040	38.537	6.29	MRK 0464		208.9730	38.5746	2.21	0.32		0.25	0.07	0.0501	44.12	Sy1.5
235	SWIFT J1413.2−6520	213.298	−65.340	43.42	Circinus Galaxy		213.2913	−65.3390	27.48	0.57		0.35	0.01	0.0014	42.10	AGN
236	SWIFT J1413.2−0312	213.308	−3.211	44.78	NGC 5506		213.3119	−3.2075	25.64	0.50		0.35	0.01	0.0062	43.34	Sy1.9
237	SWIFT J1417.9+2507	214.477	25.168	13.73	NGC 5548		214.4981	25.1368	8.08	0.50		0.41	0.03	0.0172	43.73	Sy1.5
238	SWIFT J1419.0−2639	214.827	−26.645	7.07	ESO 511-G030		214.8434	−26.6447	4.71	0.65		0.44	0.06	0.0224	43.73	Sy1
239	SWIFT J1421.6+4751	215.389	47.842	5.12	SBS 1419+480		215.3742	47.7902	2.11	0.39		0.34	0.07	0.0723	44.43	Sy1.5
240	SWIFT J1428.7+4234	217.195	42.667	8.52	1ES 1426+428		217.1361	42.6724	2.33	0.29		0.26	0.05	0.1290	45.01	BL Lac
241	SWIFT J1436.4+5846	219.079	58.773	5.06	MRK 0817		219.0920	58.7943	2.21	0.36		0.35	0.07	0.0314	43.70	Sy1.5
242	SWIFT J1442.5−1715	220.607	−17.239	14.57	NGC 5728		220.5997	−17.2532	10.54	0.71		0.43	0.03	0.0093	43.31	Sy2
243	SWIFT J1451.0−5540	222.692	−55.608	7.64	WKK 4374		222.8881	−55.6773	4.36		AB	0.39		0.0180	43.50	Sy2
244	"	"	"	"	2MFGC 12018		222.3030	−55.6050	3.71		AB	0.47		?		Galaxy
245	SWIFT J1453.4−5524	223.440	−55.320	6.20	1RXS J145341.1−552146	IGR J14515−5542	223.4558	−55.3622	2.28	0.35	B	0.10	0.08			CV/AM Her
246	SWIFT J1455.0−5133	223.758	−51.550	5.09	WKK 4438		223.8230	−51.5710	2.02	0.54		0.34	0.11	0.0160	43.07	NLSy1
247	SWIFT J1457.8−4308	224.453	−43.140	5.99	IC 4518A		224.4216	−43.1321	3.29	0.52		0.24	0.07	0.0163	43.29	Sy2
248	SWIFT J1504.2+1025	226.013	10.455	6.33	Mrk 841		226.0050	10.4378	2.93	0.53		0.37	0.06	0.0364	43.96	Sy1
249	SWIFT J1506.7+0353	226.612	3.868	5.42	2MASX J15064412+0351444		226.6840	3.8620	2.12		AB	0.30		0.0377	43.84	Sy2
250	"	"	"	"	MRK 1392		226.4860	3.7070	1.99		AB	0.34		0.0361	43.78	Sy1
251	SWIFT J1512.9−0905	228.230	−9.087	7.45	PKS 1510−08		228.2106	−9.1000	6.56	0.76		0.48	0.06	0.3600	46.46	QSO
252	SWIFT J1513.8−8125	228.299	−81.429	5.29	2MASX J15144217−8123377		228.6751	−81.3939	2.56	0.48		0.32	0.07	0.0684	44.46	Sy1.9
253	SWIFT J1514.0−5909	228.509	−59.145	39.85	PSR B1509−58	Cir pulsar	228.4813	−59.1358	27.50	0.72		0.42	0.01			PSR/PWN
254	SWIFT J1515.0+4205	228.755	42.076	5.12	NGC 5899		228.7635	42.0499	2.15	0.45		0.43	0.09	0.0086	42.54	Sy2
255	SWIFT J1515.2+1223	228.788	12.384	4.86	SWIFT J1515.2+1223	SWIFT J151447.0+122244	228.6958	12.3789	2.05	0.54		0.30	0.09	?		
256	SWIFT J1520.7−5710	230.175	−57.166	40.35	BR Cir	Cir X-1	230.1703	−57.1667	13.76	0.26		0.03	0.01			LMXB
257	SWIFT J1533.2−0836	233.298	−8.629	5.33	MCG −01-40-001		233.3363	−8.7005	3.76	0.57		0.34	0.07	0.0227	43.64	Sy2
258	SWIFT J1535.9+5751	233.983	57.853	5.25	Mrk 290		233.9682	57.9026	2.55	0.41		0.33	0.06	0.0296	43.71	Sy1
259	SWIFT J1542.4−5223	235.608	−52.379	69.23	QV Nor	H 1538−522	235.5971	−52.3861	30.41	0.38		0.09	0.01			HMXB
260	SWIFT J1546.3+6928	236.601	69.461	5.77	2MASX J15462424+6929102		236.6014	69.4861	15.46	0.55	B	0.26	0.01	0.0380	44.72	Sy2
261	"	"	"	"	1RXS J154534.5+692925		236.3938	69.4903	1.69		A	0.20		?		SRC/X-RAY
262	SWIFT J1547.9−6234	236.973	−62.570	17.09	1XMM J154754.7−623404	4U 1543−62	236.9762	−62.5698	5.70	0.29		0.06	0.03			LMXB/NS

Table 5
(Continued)

#	BAT Name[a]	R.A.[b]	Decl.	S/N	Counterpart Name	Other Name	Ctpt R.A.[c]	Ctpt Decl.	Flux[d]	Error	C[e]	Hrat[f]	Herr	Redshift[g]	Lum[h]	Type
263	SWIFT J1548.2−4529	237.044	−45.491	18.06	NY Lup	IGR J15479−4529	237.0608	−45.4778	10.14	0.55		0.29	0.02			CV/DQ Her
264	SWIFT J1548.5−1344	237.105	−13.735	5.92	NGC 5995		237.1040	−13.7578	4.51	0.61		0.36	0.07	0.0252	43.81	Sy2
265	SWIFT J1558.4+2716	239.610	27.259	8.42	ABELL 2142		239.5672	27.2246	2.39	0.32		0.23	0.05	0.0909	44.69	Galaxy cluster
266	SWIFT J1559.5+2556	239.882	25.926	14.80	T CrB	Nova CrB 1866/1946	239.8757	25.9202	6.40	0.36		0.25	0.02			Symb/WD
267	SWIFT J1613.2−6043	243.126	−60.631	7.41	WKK 6092		242.9642	−60.6319	3.99	0.58		0.30	0.06	0.0156	43.34	Sy1
268	SWIFT J1612.7−5225	243.179	−52.421	97.13	QX Nor	4U 1608−522	243.1792	−52.4231	49.82	0.52		0.27	0.00			LMXB
269	SWIFT J1617.1−4959	244.283	−49.990	5.70	1RXS J161637.1−495847	IGR J16167−4957	244.2800	−49.9600	2.08	0.38		0.10	0.09			CV
270	SWIFT J1619.2−4945	244.887	−49.722	8.71	2MASS J16193220−4944305	IGR J16195−4945	244.8842	−49.7418	3.55	0.43		0.15	0.06	?		Possible HMXB/FXT
271	SWIFT J1619.6−2807	244.903	−28.125	7.75	USNO-A2.0 U0600−20227091	IGR J16194−2810	244.8875	−28.1272	4.74	0.45		0.19	0.05			Symb/NS
272	SWIFT J1619.9−1538	244.980	−15.641	4635.67	V808 Sco	Sco X-1	244.9795	−15.6402	1821.87	0.30		0.01	0.00			LMXB/NS
273	SWIFT J1621.2+8104	245.090	81.040	6.74	CGCG 367−009		244.8302	81.0465	3.20	0.52		0.47	0.06	0.0274	43.74	Sy2
274	SWIFT J1620.7−5129	245.175	−51.478	9.64	2MASS J16203698−5130363	IGR J16207−5129	245.1542	−51.5100	4.34	0.47		0.22	0.05			HMXB
275	SWIFT J1626.5−5157	246.623	−51.951	9.09	SWIFT J162636.2−515634	SWIFT J1626.6−5156	246.6510	−51.9428	3.84	0.36		0.11	0.05			XRB/NS
276	SWIFT J1628.0−4913	246.992	−49.211	25.04	4U 1624−490	4U 1624−490/ Big dipper	247.0118	−49.1985	8.95	0.27		0.04	0.02			LMXB/NS
277	SWIFT J1628.1+5145	247.059	51.733	10.02	Mrk 1498		247.0169	51.7754	4.37	0.44		0.39	0.04	0.0547	44.49	Sy1.9
278	SWIFT J1631.8−4849	247.960	−48.821	76.77	IGR J16318−4848		247.9667	−48.8083	48.15	0.54		0.27	0.01			HMXB/NS
279	SWIFT J1632.0−4752	248.010	−47.863	47.01	AX J1631.9−4752	IGR J16320−4751; HESS J1632−478	248.0079	−47.8742	26.52	0.46		0.17	0.01			PSR
280	SWIFT J1632.3−6728	248.076	−67.464	64.78	4U 1626−67		248.0700	−67.4619	26.33	0.34		0.04	0.01			LMXB
281	SWIFT J1638.5−6424	249.619	−64.400	5.94	TrA Cluster		249.5671	−64.3472	2.36	0.34		0.00	0.09	0.0508	44.16	Galaxy cluster
282	SWIFT J1639.1−4642	249.767	−46.707	17.44	IGR J16393−4643		249.7583	−46.6767	9.37	0.38		0.06	0.02			Symb/NS
283	SWIFT J1641.0−5345	250.238	−53.751	100.33	V801 Ara	4U 1636−536	250.2313	−53.7514	44.22	0.44		0.18	0.00			LMXB
284	SWIFT J1641.8−4534	250.452	−45.571	11.34	IGR J16418−4532	2MASS J16415078−4532253 ?	250.4375	−45.5200	7.27	0.45		0.13	0.03			SRC/GAMMA
285	SWIFT J1643.2+3951	250.797	39.856	6.43	3C 345		250.7450	39.8103	3.34	0.64		0.47	0.07	0.5928	46.69	HPQ
286	SWIFT J1645.8−4537	251.445	−45.613	175.21	GX 340+0	4U 1642−45	251.4488	−45.6111	77.93	0.32	B	0.02	0.00			LMXB/NS
287	SWIFT J1648.0−3037	252.048	−30.594	10.15	2MASX J16481523−3035037		252.0635	−30.5845	8.36	0.70		0.40	0.04	0.0310	44.27	Sy1
288	SWIFT J1648.2−4510	252.052	−45.160	12.36	2MASS J16480656−4512068	IGR J16479−4514	251.9958	−45.2167	8.73		AB	0.22				HMXB/fast trans
289	"	"	"	"	IGR J16465−4507		251.6480	−45.1170	2.84		AB	0.15				
290	SWIFT J1649.5−4350	252.366	−43.826	9.25	2MASS J16492695−4349090	IGR J16493−4348	252.3375	−43.8100	4.85	0.45		0.19	0.04			XRB/NS
291	SWIFT J1650.5+0434	252.625	4.533	5.39	LEDA 214543		252.6781	4.6050	3.38	0.61		0.48	0.09	0.0321	43.90	Sy2
292	SWIFT J1652.9+0223	253.235	2.399	9.38	NGC 6240		253.2454	2.4009	7.30	0.62		0.44	0.04	0.0245	44.00	Sy2
293	SWIFT J1654.0+3946	253.444	39.750	14.88	Mrk 501		253.4676	39.7602	5.46	0.39		0.27	0.03	0.0337	44.15	BL Lac
294	SWIFT J1654.0−3951	253.496	−39.844	49.78	GRO J1655−40		253.5006	−39.8458	35.24	0.65		0.35	0.01			LMXB/BH
295	SWIFT J1656.0−5203	253.992	−52.057	5.75	1RXS J165605.6−520345		254.0234	−52.0614	3.81	0.77		0.41	0.08	0.0540	44.42	Sy1.2
296	SWIFT J1656.3−3302	254.016	−33.059	8.86	2MASS J16561677−3302127	SWIFT J1656.3−3302	254.0699	−33.0369	8.50	0.81		0.47	0.05	2.4000	48.58	Blazar
297	SWIFT J1657.8+3520	254.459	35.340	281.06	HZ Her	Her X-1	254.4576	35.3424	90.54	0.28		0.07	0.00			LMXB/NS
298	SWIFT J1700.3−4225	255.077	−42.417	6.10	AX J1700.2−4220		255.1050	−42.3170	3.46	0.50		0.25	0.07			
299	SWIFT J1700.8−4139	255.206	−41.658	168.95	Roche star 10B	OAO 1657−415	255.1996	−41.6731	97.40	0.50		0.23	0.00			HMXB/NS
300	SWIFT J1701.0−4611	255.252	−46.184	57.73	XTE J1701−462		255.2436	−46.1857	24.02	0.30		0.01	0.01			LMXB
301	SWIFT J1702.9−4848	255.716	−48.792	38.26	V821 Ara	GX 339−4	255.7063	−48.7897	38.26	0.80		0.48	0.01			LMXB
302	SWIFT J1703.9−3751	255.987	−37.845	581.69	V884 Sco	4U 1700−377	255.9866	−37.8441	362.89	0.49		0.23	0.00			HMXB/NS
303	SWIFT J1705.8−3625	256.438	−36.422	259.90	V1101 Sco	GX 349+2	256.4354	−36.4231	117.09	0.31		0.00	0.00			LMXB/NS
304	SWIFT J1706.3−4302	256.563	−43.038	73.91	Ara X-1	4U 1702−429	256.5638	−43.0358	40.43	0.48		0.22	0.00			LMXB/NS
305	SWIFT J1706.6−6146	256.622	−61.771	5.52	SWIFT J179616.4−614240	IGR J17062−6143	256.5677	−61.7113	3.81	0.63		0.39	0.07			
306	SWIFT J1706.8+2358	256.707	23.962	7.49	V934 Her	4U 1700+24	256.6438	23.9718	3.93	0.46		0.32	0.05			LMXB/NS

Table 5
(Continued)

#	BAT Name[a]	R.A.[b]	Decl.	S/N	Counterpart Name	Other Name	Ctpt R.A.[c]	Ctpt Decl.	Flux[d]	Error	C[e]	Hrat[f]	Herr	Redshift[g]	Lum[h]	Type
307	SWIFT J1708.7−4009	257.163	−40.152	5.47	RX J170849.0−400910		257.2050	−40.1530	5.06	0.86		0.55	0.10			NS/AXP
308	SWIFT J1708.9−3219	257.216	−32.309	8.09	2XMM J170854.2−321858	4U 1705−32	257.2267	−32.3160	6.16	0.68		0.37	0.05			LMXB
309	SWIFT J1708.9−4406	257.228	−44.106	69.48	4U 1705−440		257.2270	−44.1020	29.50	0.34		0.11	0.01			LMXB/NS
310	SWIFT J1709.8−3624	257.442	−36.404	6.33	SWIFT J170945.9−362759	IGR J17098−3628	257.4424	−36.4660	6.08		AB	0.42				SRC/GAMMA
311	"	"	"	"	IGR J17091−3624		257.2750	−36.4110	3.49		AB	0.40				SRC/GAMMA
312	SWIFT J1710.2−2807	257.546	−28.121	8.29	1RXS J171012.3−280754	XTE J1710−281	257.5513	−28.1317	5.16	0.50		0.26	0.04			LMXB
313	SWIFT J1712.4−2322	258.088	−23.367	19.03	Oph Cluster		258.1082	−23.3759	9.70	0.36		0.07	0.02	0.0280	44.24	Galaxy cluster
314	SWIFT J1712.4−4051	258.108	−40.850	7.84	1RXS J171224.8−405034	4U 1708−40	258.0958	−40.8433	3.00	0.30		0.08	0.05			LMXB
315	SWIFT J1712.6−2415	258.157	−24.250	9.45	V2400 Oph	1RXS J171236.3−241445	258.1519	−24.2457	5.27	0.42		0.16	0.04			CV/DQ Her
316	SWIFT J1712.7−3737	258.169	−37.610	11.96	1RXS J171237.1−373834	SAX J1712.6−3739	258.1417	−37.6433	7.10	0.55		0.27	0.03			LMXB/NS
317	SWIFT J1717.1−6249	259.292	−62.844	15.53	NGC 6300		259.2478	−62.8206	10.35	0.64		0.37	0.03	0.0037	42.50	Sy2
318	SWIFT J1719.5−4058	259.863	−40.971	6.32	1RXS J171935.6−410054	CXOU J171935.8−410053	259.8983	−41.0151	3.59	0.43		0.12	0.05			CV
319	SWIFT J1719.8+4858	259.950	48.971	5.22	ARP 102B		259.8104	48.9804	1.89	0.45		0.35	0.09	0.0242	43.40	Sy1 LINER
320	SWIFT J1720.1−3112	260.022	−31.207	6.99	2MASS J17200591−3116596	IGR J17200−3116	260.0254	−31.2839	3.58	0.42		0.07	0.06			HMXB
321	SWIFT J1725.2−3616	261.310	−36.267	18.54	2MASS J17251139−3616575	EXO 1722−363	261.2975	−36.2831	12.03	0.45		0.12	0.02			HMXB/NS
322	SWIFT J1725.6−3256	261.390	−32.931	5.16	IGR J17254−3257		261.3500	−32.9500	3.25	0.53		0.24	0.07			SRC/GAMMA
323	SWIFT J1727.6−3048	261.889	−30.800	52.66	4U 1722−30	4U1724−30	261.8883	−30.8019	32.40	0.51		0.24	0.01			LMXB
324	SWIFT J1730.4−0600	262.591	−6.005	10.84	1RXS J173021.5−055933	1H 1726−058	262.5896	−5.9926	6.78	0.51		0.29	0.03			CV/DQ Her
325	SWIFT J1731.7−1658	262.935	−16.961	87.04	V2216 Oph	GX 9+9	262.9342	−16.9617	35.58	0.29		0.00	0.00			LMXB/NS
326	SWIFT J1732.0−3350	262.993	−33.833	145.26	Slow burster	4U1728−33	262.9892	−33.8347	70.50	0.38		0.09	0.00			LMXB/NS
327	SWIFT J1732.0−2445	263.010	−24.745	149.22	V2116 Oph	GX 1+4	263.0090	−24.7456	109.08	0.57		0.30	0.00			HMXB/NS
328	SWIFT J1737.5−2908	264.382	−29.152	14.84	AX J1737.4−2907	GRS 1734−292	264.3512	−29.1800	12.33	0.69		0.38	0.03	0.0214	44.11	Sy1
329	SWIFT J1738.3−2700	264.573	−26.996	33.24	SLX 1735−269	SLX 1735−269	264.5667	−27.0044	24.94	0.62		0.33	0.01			LMXB/NS
330	SWIFT J1739.0−4427	264.745	−44.451	147.81	V926 Sco	4U 1735−44	264.7429	−44.4500	61.59	0.29		0.01	0.00			LMXB/NS
331	SWIFT J1740.5−3652	265.117	−36.873	5.23	IGR J17404−3655		265.1110	−36.9270	2.86	0.49		0.25	0.07			XRB
332	SWIFT J1740.5−2821	265.127	−28.350	15.92	SLX 1737−282		265.2375	−28.3100	10.20		AB	0.34				LMXB
333	"	"	"	"	CXO J170058.6−461108.6	XTE J1739−285	264.9748	−28.4963	7.68		AB	0.29				LMXB
334	SWIFT J1743.0−3619	265.753	−36.310	5.80	XTE J1743−363		265.7500	−36.3450	3.53	0.55		0.30	0.06			SRC/X-ray
335	SWIFT J1743.9−2945	265.969	−29.745	80.30	1E 1740.7−2942		265.9785	−29.7452	76.10	0.74	B	0.40	0.00			LMXB/BH
336	SWIFT J1746.0−2930	266.506	−29.492	44.90	2E1742−2929	1A 1742−294	266.5229	−29.5153	23.95		AB	0.17				LMXB
337	SWIFT J1746.1−3219	266.533	−32.316	8.02	H 1743−322		266.5650	−32.2335	5.95	0.60		0.30	0.04			LMXB
338	SWIFT J1746.3−2853	266.569	−28.885	32.02	CXOGC J174702.6−285258	SAX J1747.0−2853	266.7608	−28.8830	15.02		AB	0.25				LMXB
339	"	"	"	"	2E 1743.1−2842		266.5800	−28.7353	13.48		AB	0.19				LMXB
340	"	"	"	"	IGR J17461−2853		266.5250	−28.8820	17.33		AB	0.24				Molecular cloud?
341	"	"	"	"	SGR A*		266.4168	−29.0078	14.83		AB	0.26				Galactic center
342	SWIFT J1747.3−2722	266.822	−27.371	8.40	IGR J17473−2721		266.8253	−27.3441	7.87	0.77	B	0.42	0.05			XRB burster
343	SWIFT J1747.4−3001	266.856	−30.022	25.58	AX J1747.4−3000	SLX 1744−299	266.8579	−29.9994	14.38		AB	0.20				LMXB/NS
344	"	"	"	"	AX J1747.4−3003	SLX 1744−300	266.8558	−30.0447	15.38		AB	0.21				LMXB
345	SWIFT J1747.5−2259	266.866	−22.977	4.82	NVSS J174729−225245		266.8740	−22.8790	3.37	0.61		0.32	0.08	?		Possible QSO
346	SWIFT J1747.9−2634	266.985	−26.570	60.05	GX 3+1	4U 1744−26	266.9833	−26.5636	25.48	0.30		0.00	0.01			LMXB/NS
347	SWIFT J1748.9−3258	267.231	−32.965	6.81	2MASS J17485512−3254521	IGR J17488−3253	267.2297	−32.9145	4.88	0.67		0.33	0.06	0.0200	43.65	Sy1
348	SWIFT J1749.4−2820	267.351	−28.330	17.72	SWIFT J174938.1−282116.9	IGR J17497−2821	267.4088	−28.3547	16.34	0.78		0.45	0.02			LMXB
349	SWIFT J1750.2−3704	267.556	−37.068	17.53	4U 1746−37		267.5529	−37.0522	7.33	0.32		0.03	0.02			LMXB/NS
350	SWIFT J1753.5−0127	268.364	−1.448	150.99	SWIFT J175328.5−012704	SWIFT J1753.5−0127	268.3679	−1.4525	129.95	0.72		0.45	0.00			LMXB/ BHC

Table 5
(Continued)

#	BAT Name[a]	R.A.[b]	Decl.	S/N	Counterpart Name	Other Name	Ctpt R.A.[c]	Ctpt Decl.	Flux[d]	Error	C[e]	Hrat[f]	Herr	Redshift[g]	Lum[h]	Type
351	SWIFT J1759.6−2201	269.908	−22.020	10.09	XTE J1759−220	IGRJ17597−2201	269.9417	−22.0150	6.89	0.49		0.19	0.03			LMXB
352	SWIFT J1801.1−2505	270.285	−25.077	238.67	GX 5−1		270.2842	−25.0792	127.44	0.33		0.01	0.00			LMXB/NS
353	SWIFT J1801.2−2545	270.304	−25.745	173.08	1XMM J180112.7−254440	GRS 1758−258	270.3012	−25.7433	196.30	0.79		0.44	0.00			LMXB/BH
354	SWIFT J1801.6−2031	270.398	−20.523	113.79	GX 9+1		270.3846	−20.5289	53.19	0.33		0.00	0.00			LMXB/NS
355	SWIFT J1808.5−2023	272.116	−20.377	7.12	CXOU J180839.3−202439	SGR 1806−20	272.1638	−20.4110	6.76	0.85		0.43	0.06			SGR
356	SWIFT J1814.5−1710	273.634	−17.160	79.81	V5512 Sgr	GX 13+1	273.6315	−17.1574	34.91	0.32		0.04	0.00			LMXB/NS
357	SWIFT J1815.1−1206	273.778	−12.096	81.92	4U 1812−12		273.8000	−12.0833	58.17	0.65		0.35	0.01			LMXB/NS
358	SWIFT J1816.0−1402	274.005	−14.037	265.05	NP Ser	GX 17+2	274.0058	−14.0364	127.18	0.31		0.01	0.00			LMXB/NS
359	SWIFT J1817.7−3302	274.426	−33.037	19.21	XTE J1817−330		274.4314	−33.0188	15.15	0.62		0.33	0.02			XRB/BHC
360	SWIFT J1822.3+6422	275.574	64.372	5.35	[HB89] 1821+643		275.4888	64.3434	1.74	0.35		0.26	0.08	0.2970	45.69	Sy1
361	SWIFT J1823.7−3022	275.919	−30.359	170.72	4U 1820−30		275.9186	−30.3611	85.23	0.35		0.02	0.00			LMXB/NS
362	SWIFT J1824.3−5623	276.077	−56.385	8.04	IC 4709		276.0808	−56.3692	5.30	0.67		0.37	0.05	0.0169	43.53	Sy2
363	SWIFT J1825.3−0002	276.337	−0.031	14.06	4U 1822−000		276.3421	−0.0122	5.38	0.27		0.00	0.03			LMXB/NS
364	SWIFT J1825.8−3706	276.451	−37.106	101.08	V691 CrA	4U 1822−371	276.4450	−37.1053	45.15	0.35		0.05	0.00			LMXB
365	SWIFT J1829.3+4840	277.328	48.667	4.82	3C 380		277.3820	48.7460	2.56	0.54		0.47	0.10	0.6920	46.73	Sy1.5 LPQ
366	SWIFT J1829.5−2348	277.369	−23.797	244.65	V4634 Sgr	Ginga 1826−24	277.3675	−23.7969	175.79	0.61		0.30	0.00			LMXB/NS
367	SWIFT J1830.8+0928	277.682	9.463	6.72	2MASX J18305065+0928414		277.7110	9.4783	3.94	0.64		0.36	0.06	0.0190	43.51	Sy2
368	SWIFT J1833.5−1034	278.364	−10.569	13.54	SNR G21.5−00.9		278.3833	−10.5600	8.63	0.63		0.33	0.03			SNR
369	SWIFT J1833.7−2103	278.423	−21.044	8.52	PKS 1830−21		278.4162	−21.0611	9.41	0.91		0.51	0.05	2.5000	48.67	Blazar
370	SWIFT J1835.0+3240	278.755	32.693	16.94	3C 382		278.7641	32.6963	8.42	0.50		0.35	0.02	0.0579	44.83	Sy1
371	SWIFT J1835.8−3300	278.943	−32.992	33.38	XB 1832−330		278.9338	−32.9914	24.31	0.63		0.36	0.01			LMXB/NS
372	SWIFT J1837.1−5924	279.280	−59.403	5.56	FAIRALL 0049		279.2429	−59.4024	2.93	0.54		0.30	0.08	0.0202	43.43	Sy2
373	SWIFT J1838.0−0656	279.500	−6.941	8.21	PSR J1838−0655	AX J1838.0−0655/ HESS J1837−069	279.4279	−6.9275	4.69	0.67		0.41	0.07			PSR/PWN
374	SWIFT J1838.4−6524	279.613	−65.428	17.29	ESO 103−035		279.5848	−65.4276	11.14	0.59		0.35	0.02	0.0133	43.64	Sy2
375	SWIFT J1840.0+0502	279.989	5.040	98.36	MM Ser	Ser X-1	279.9896	5.0358	33.58	0.24		0.01	0.00			LMXB/NS
376	SWIFT J1841.4−0457	280.357	−4.958	11.30	AXP 1E 1841−045	Kes 73	280.3300	−4.9364	10.89	0.81		0.54	0.04			AXP
377	SWIFT J1842.0+7945	280.569	79.781	25.24	3C 390.3		280.5375	79.7714	10.97	0.46		0.39	0.02	0.0561	44.92	Sy1
378	SWIFT J1844.5−6225	281.136	−62.423	6.93	Fairall 0051		281.2249	−62.3648	4.57	0.66		0.44	0.07	0.0142	43.31	Sy1
379	SWIFT J1844.9−0437	281.224	−4.610	5.19	AX J1845.0−0433	IGR J18450−0435	281.2588	−4.5653	3.46	0.67		0.34	0.07			HMXB
380	SWIFT J1845.7+0052	281.415	0.862	11.48	Ginga 1843+00		281.4125	0.8917	6.28	0.52		0.27	0.04			HMXB
381	SWIFT J1846.4−0255	281.589	−2.922	4.88	AX J1846.4−0258		281.6020	−2.9740	3.45	0.60		0.39	0.08			PSR
382	SWIFT J1848.3−0310	282.077	−3.174	14.82	IGR J18483−0311		282.0750	−3.1617	9.03	0.56		0.29	0.03			HMXB/NS
383	SWIFT J1853.2−0842	283.289	−8.694	26.23	4U 1850−086		283.2703	−8.7057	14.72	0.59		0.33	0.02			LMXB/NS
384	SWIFT J1854.9−3110	283.732	−31.168	18.77	V1223 Sgr		283.7593	−31.1635	9.71	0.46		0.13	0.02			CV/DQ Her
385	SWIFT J1855.5−0237	283.883	−2.613	39.39	XTE J1855−026		283.8804	−2.6067	21.54	0.48		0.25	0.01			HMXB/NS
386	SWIFT J1856.2+1539	284.048	15.658	5.47	2E 1853.7+1534		284.0053	15.6349	3.16	0.53		0.39	0.07	0.0840	44.74	Sy1
387	SWIFT J1856.7−7834	284.171	−78.559	5.06	2MASX J18570768−7828212		284.2823	−78.4725	2.47		AB	0.42		0.0420	44.01	Sy1
388	"	"	"	"	[HB91] 1846−786		283.4860	−78.5400	1.75		AB	0.49		0.0760	44.39	Sy1
389	SWIFT J1858.8+0329	284.693	3.486	5.12	XTE J1858+034		284.6790	3.4340	2.20	0.32		0.03	0.08			HMXB/NS
390	SWIFT J1900.2−2455	285.041	−24.919	79.77	HETE J1900.1−2455		285.0360	−24.9205	55.74	0.64		0.33	0.00			LMXB/msPSR
391	SWIFT J1901.7+0128	285.414	1.465	10.25	XTE J1901+014		285.4208	1.4385	6.73	0.60		0.34	0.04			SRC/GAMMA
392	SWIFT J1907.3−2050	286.823	−20.836	5.78	V1082 Sgr		286.8411	−20.7808	2.75	0.53		0.25	0.08			CV
393	SWIFT J1909.6+0950	287.404	9.832	66.62	4U 1907+09		287.4079	9.8303	26.23	0.34		0.05	0.01			HMXB/NS

Table 5
(Continued)

#	BAT Name[a]	R.A.[b]	Decl.	S/N	Counterpart Name	Other Name	Ctpt R.A.[c]	Ctpt Decl.	Flux[d]	Error	C[e]	Hrat[f]	Herr	Redshift[g]	Lum[h]	Type
394	SWIFT J1910.8+0736	287.698	7.602	58.10	2MASS J19104821+0735516	4U 1909+07	287.7000	7.5983	25.79	0.46		0.23	0.01			HMXB/NS
395	SWIFT J1911.2+0034	287.811	0.560	21.25	Aql X-1		287.8167	0.5850	13.17	0.56		0.32	0.02			LMXB
396	SWIFT J1911.8+0459	287.954	4.977	27.20	SS 433		287.9565	4.9827	12.01	0.43		0.21	0.02			uQuasar
397	SWIFT J1914.1+0953	288.520	9.876	31.99	2MASS J19140422+0952577	IGR J19140+0951	288.5083	9.8883	16.82	0.46		0.23	0.01			HMXB
398	SWIFT J1915.2+1057	288.799	10.946	840.73	GRS 1915+105		288.7983	10.9456	386.66	0.40		0.17	0.00			LMXB/BH
399	SWIFT J1918.8−0514	289.700	−5.235	31.84	V1405 Aql	4U 1916−053	289.6995	−5.2381	16.17	0.51		0.22	0.01			LMXB/NS
400	SWIFT J1921.0+4357	290.239	43.952	10.36	ABELL 2319		290.1889	43.9619	2.62	0.26		0.10	0.05	0.0557	44.29	Galaxy cluster
401	SWIFT J1921.5−5843	290.363	−58.711	8.23	ESO 141- G 055		290.3090	−58.6703	5.27	0.58		0.32	0.04	0.0360	44.20	Sy1
402	SWIFT J1922.7−1716	290.645	−17.274	20.96	SWIFT J1922.7−1716	SWIFT J192237.0−171702	290.6542	−17.2842	14.69	0.67		0.33	0.02			XRB/ uQuasar?
403	SWIFT J1924.5+5017	291.114	50.289	7.87	CH Cyg	2MASS J19243305+5014289	291.1378	50.2414	2.26	0.24		0.08	0.06			Symb/WD
404	SWIFT J1930.5+3414	292.593	34.208	7.63	2MASX J19301380+3410495		292.5575	34.1805	3.26	0.52		0.40	0.07	0.0629	44.49	Sy1
405	SWIFT J1933.9+3258	293.437	32.970	5.43	2MASS J19334715+3254259	1RXS J193347.6+325422	293.4483	32.9061	2.30	0.49		0.37	0.08	0.0578	44.26	Sy1.2
406	SWIFT J1940.3−1027	295.063	−10.446	10.25	V1432 Aql		295.0478	−10.4236	5.40	0.49		0.21	0.04			CV/AM Her
407	SWIFT J1942.6−1024	295.658	−10.349	11.28	NGC 6814		295.6694	−10.3235	7.82	0.69		0.38	0.04	0.0052	42.67	Sy1.5
408	SWIFT J1942.8+3220	295.687	32.329	4.81	V2491 Cyg		295.7582	32.3205	1.84	0.54		0.38	0.11			CV/Nova
409	SWIFT J1943.5+2120	295.950	21.290	7.94	SWIFT J194353.0+212119	IGR J19443+2117	295.9842	21.3064	4.42	0.55		0.38	0.05			SRC/X-ray
410	SWIFT J1947.1+4448	296.782	44.808	5.13	2MASX J19471938+4449425		296.8307	44.8284	2.44	0.52		0.40	0.09	0.0539	44.23	Sy2
411	SWIFT J1949.5+3012	297.404	30.179	20.98	KS 1947+300		297.3771	30.2067	8.18	0.38		0.24	0.02			HMXB/NS
412	SWIFT J1952.4+0237	298.055	2.502	5.45	3C 403		298.0660	2.5070	4.27	0.81		0.55	0.09	0.0590	44.55	Sy2
413	SWIFT J1955.7+3206	298.929	32.095	97.31	TYC 2673-2004-1	4U 1954+31	298.9264	32.0970	35.52	0.33		0.17	0.00			LMXB
414	SWIFT J1958.4+3512	299.591	35.201	4304.23	Cyg X-1		299.5903	35.2016	2245.76	0.52		0.41	0.00			HMXB/BH
415	SWIFT J1959.4+4044	299.857	40.734	25.99	Cygnus A		299.8682	40.7339	12.23	0.49		0.37	0.02	0.0561	44.96	Sy2
416	SWIFT J1959.6+6507	299.970	65.195	11.23	QSO B1959+650	1ES 1959+650	299.9994	65.1485	3.87	0.36		0.24	0.04	0.0470	44.30	BL Lac
417	SWIFT J2000.6+3210	300.144	32.183	7.87	USNO-A2.0 1200-14131541	2MASS J20002185+3211232	300.0913	32.1894	3.25	0.40		0.26	0.05			HMXB
418	SWIFT J2009.0−6103	302.263	−61.072	8.71	NGC 6860		302.1954	−61.1002	6.50	0.73		0.40	0.05	0.0149	43.51	Sy1
419	SWIFT J2018.5+4043	304.636	40.714	5.36	2MASX J20183871+4041003	IGR J20187+4041	304.6613	40.6834	3.36	0.55		0.47	0.08	0.0144	43.19	Sy2
420	SWIFT J2028.5+2543	307.149	25.742	14.88	MCG +04-48-002		307.1461	25.7333	8.77	0.59		0.45	0.03	0.0139	43.58	Sy2
421	SWIFT J2032.3+3738	308.067	37.636	276.33	EXO 2030+375		308.0633	37.6375	99.67	0.35		0.21	0.00			HMXB/NS
422	SWIFT J2032.4+4057	308.107	40.958	753.06	Cyg X-3	V1521 Cyg	308.1074	40.9578	238.90	0.32		0.16	0.00			HMXB/NS
423	SWIFT J2033.4+2147	308.357	21.779	6.48	4C +21.55		308.3835	21.7729	3.26	0.49		0.38	0.06	0.1735	45.44	QSO
424	SWIFT J2037.2+4151	309.261	41.839	7.02	SWIFT J203705.78−415005.1	SWIFT J2037.2+4151	309.3000	41.8500	1.71	0.19		0.00	0.07			transient
425	SWIFT J2042.3+7507	310.574	75.110	13.49	4C +74.26		310.6554	75.1340	5.02	0.41		0.32	0.03	0.1040	45.14	Sy1
426	SWIFT J2044.0+2832	311.007	28.550	5.83	RX J2044.0+2833		311.0188	28.5534	2.53	0.46		0.35	0.07	0.0500	44.17	Sy1
427	SWIFT J2044.2−1045	311.061	−10.734	14.89	Mrk 509		311.0406	−10.7235	9.44	0.68		0.37	0.03	0.0344	44.41	Sy1.2
428	SWIFT J2052.0−5704	312.988	−57.062	10.93	IC 5063		313.0098	−57.0688	8.59	0.72		0.40	0.04	0.0114	43.39	Sy2
429	SWIFT J2114.4+8206	318.331	82.079	9.44	2MASX J21140128+8204483		318.5049	82.0801	4.21	0.51		0.44	0.05	0.0840	44.87	Sy1
430	SWIFT J2117.9+5140	319.466	51.668	6.88	2MASX J21174741+5138523		319.4480	51.6483	3.14	0.52		0.46	0.06	?		Galaxy
431	SWIFT J2118.9+3336	319.717	33.593	4.84	2MASX J21192912+3332566		319.8714	33.5491	1.53	0.44		0.39	0.12	0.0507	43.97	Sy1
432	SWIFT J2123.2+4220	320.796	42.337	4.99	V2069 Cyg		320.9370	42.3010	1.21	0.29		0.10	0.12			CV
433	SWIFT J2123.6+2500	320.903	24.999	4.86	3C 433		320.9356	25.0700	1.74	0.44		0.29	0.08	0.1016	44.66	Sy2 NLRG
434	SWIFT J2124.6+5057	321.165	50.974	43.15	4C 50.55	IGR J21247+5058	321.1641	50.9738	17.81	0.47		0.39	0.01	0.0200	44.21	BLRG, not Sy 1
435	SWIFT J2127.4+5654	321.931	56.964	9.99	SWIFT J212745.58+565635.6	IGR J21277+5656	321.9373	56.9444	3.87	0.39		0.25	0.04	0.0147	43.27	Sy1
436	SWIFT J2129.9+1210	322.484	12.175	22.11	NGC 7078 AC 211	4U 2129+12	322.4929	12.1674	9.16	0.45		0.27	0.02			LMXB
437	SWIFT J2132.0−3343	322.996	−33.763	8.26	6dF J2132022−334254		323.0092	−33.7150	5.55	0.74		0.42	0.05	0.0293	44.04	Sy1

Table 5
(Continued)

#	BAT Name[a]	R.A.[b]	Decl.	S/N	Counterpart Name	Other Name	Ctpt R.A.[c]	Ctpt Decl.	Flux[d]	Error	C[e]	Hrat[f]	Herr	Redshift[g]	Lum[h]	Type
438	SWIFT J2133.8+5109	323.455	51.143	16.49	RX J2133.7+5107		323.4320	51.1236	5.23	0.33		0.19	0.03			CV/DQ Her
439	SWIFT J2135.5−6222	323.934	−62.365	7.37	1RXS J213623.1−622400		324.0963	−62.4002	3.88	0.57		0.35	0.06	0.0588	44.51	Sy1
440	SWIFT J2156.1+4728	324.047	47.507	6.11	2MASX J21355399+4728217		323.9750	47.4727	2.68	0.47	B	0.41	0.07	0.0250	43.58	Sy1
441	"	"	"	"	IGR J21347+4737		323.8460	47.5770	1.50		A	0.44				XRB
442	SWIFT J2142.6+4335	325.660	43.576	13.88	SS Cyg		325.6784	43.5861	4.57	0.33		0.18	0.03			CV/Dwarf N
443	SWIFT J2144.7+3819	326.168	38.319	257.42	Cyg X-2		326.1717	38.3217	59.99	0.18		0.02	0.00			LMXB/NS
444	SWIFT J2152.0−3030	327.956	−30.485	12.42	PKS 2149−306		327.9814	−30.4649	10.58	0.96		0.54	0.04	2.3450	48.65	Blazar
445	SWIFT J2200.9+1032	330.180	10.578	6.16	MRK 520		330.1724	10.5524	3.58	0.64		0.43	0.07	0.0266	43.76	Sy1.9
446	SWIFT J2201.9−3152	330.514	−31.878	27.37	NGC 7172		330.5080	−31.8698	18.11	0.70		0.42	0.02	0.0087	43.48	Sy2
447	SWIFT J2202.8+4215	330.699	42.244	7.72	BL Lac		330.6804	42.2778	4.40	0.51		0.44	0.06	0.0686	44.70	BL Lac
448	SWIFT J2208.0+5431	331.991	54.517	61.64	BD+53 2790	4U 2206+54	331.9843	54.5185	22.44	0.40		0.28	0.01			HMXB/NS
449	SWIFT J2209.4−4711	332.397	−47.130	8.06	NGC 7213		332.3177	−47.1667	5.75	0.67		0.44	0.05	0.0058	42.64	Sy1.5
450	SWIFT J2217.5−0812	334.483	−8.357	13.02	FO AQR		334.4810	−8.3513	5.85	0.36		0.11	0.03			CV/DQ Her
451	SWIFT J2223.8+1143	335.964	11.764	5.71	MCG +02-57-002		335.9380	11.8360	2.08	0.45		0.32	0.09	0.0290	43.60	Sy1.5
452	SWIFT J2224.0−0208	335.995	−2.128	7.62	3C 445		335.9566	−2.1034	4.37	0.58		0.40	0.05	0.0562	44.52	Sy2
453	SWIFT J2229.9+6646	337.494	66.774	5.37	87GB 222741.2+663124		337.2999	66.7846	2.79	0.61		0.51	0.08	0.1130	44.96	Sy1
454	SWIFT J2232.7+1140	338.184	11.661	6.20	[HB89] 2230+114		338.1517	11.7308	4.17	0.65		0.53	0.07	1.0370	47.38	Blazar HP
455	SWIFT J2235.9−2602	338.920	−26.093	9.31	NGC 7314		338.9426	−26.0503	4.63	0.59		0.37	0.05	0.0048	42.37	Sy1.9
456	SWIFT J2235.9+3358	339.054	33.953	8.35	NGC 7319		339.0148	33.9757	3.96	0.52		0.41	0.05	0.0225	43.66	Sy2
457	SWIFT J2236.7−1233	339.169	−12.558	6.41	MRK 0915		339.1938	−12.5452	4.99	0.71		0.49	0.07	0.0241	43.82	Sy1
458	SWIFT J2246.0+3941	341.443	39.680	9.43	3C 452		341.4532	39.6877	3.78	0.48		0.37	0.05	0.0811	44.79	Sy2
459	SWIFT J2251.9+2215	343.052	22.275	5.14	MG3 J225155+2217		342.9729	22.2937	3.11	0.63		0.52	0.09	3.6680	48.59	QSO
460	SWIFT J2253.9+1608	343.495	16.142	26.13	3C 454.3		343.4906	16.1482	15.89	0.65		0.53	0.02	0.8590	47.76	Blazar
461	SWIFT J2254.1−1734	343.514	−17.581	17.90	MR 2251−178		343.5242	−17.5819	9.17	0.53		0.35	0.02	0.0640	44.96	Sy1
462	SWIFT J2255.4−0309	343.855	−3.149	8.83	AO Psc	3A 2253−033	343.8249	−3.1779	2.92	0.28		0.07	0.06			CV/DQ Her
463	SWIFT J2258.9+4054	344.716	40.911	6.14	UGC 12282		344.7312	40.9315	2.49	0.50		0.38	0.07	0.0170	43.21	Sy1.9
464	SWIFT J2259.7+2458	344.905	24.911	7.17	KAZ 320		344.8871	24.9182	2.88	0.51		0.37	0.07	0.0345	43.90	Sy1
465	SWIFT J2303.3+0852	345.786	8.898	15.16	NGC 7469		345.8151	8.8740	6.66	0.44		0.32	0.03	0.0163	43.60	Sy1.2
466	SWIFT J2304.8−0843	346.174	−8.675	18.38	Mrk 926		346.1811	−8.6857	10.17	0.57		0.39	0.02	0.0469	44.72	Sy1.5
467	SWIFT J2318.4−4223	349.631	−42.357	16.24	NGC 7582		349.5979	−42.3706	7.92	0.55		0.40	0.03	0.0052	42.68	Sy2
468	SWIFT J2319.0+0016	349.738	0.265	9.70	NGC 7603		349.7359	0.2440	4.70	0.51		0.34	0.04	0.0295	43.97	Sy1.5
469	SWIFT J2319.4+2619	349.867	26.352	5.14	MRK 322		350.0130	26.2160	0.64		A	0.19		0.0266	43.02	Galaxy
470	"	"	"	"	UGC 12515		349.9630	26.2630	1.28	0.37	B	0.24	0.11	0.0265	43.31	Galaxy
471	"	"	"	"	SWIFT J231930.4+261517		349.8765	26.2548	0.28		A	0.13				CV/AM Her
472	SWIFT J2323.4+5849	350.857	58.813	22.84	Cas A		350.8500	58.8150	6.78	0.32		0.19	0.02			SNR
473	SWIFT J2325.5−3827	351.358	−38.440	5.64	LCRS B232242.2−384320		351.3508	−38.4470	2.41	0.47		0.27	0.07	0.0359	43.86	Sy1
474	SWIFT J2325.8+2152	351.443	21.871	4.85	2MASX J23255427+2153142		351.4760	21.8870	1.63	0.42		0.22	0.10	0.1200	44.79	Sy1
475	SWIFT J2327.6+0629	351.912	6.451	4.92	SWIFT J2327.6+0629		351.9350	6.4180	2.55	0.62		0.40	0.09	?		

Table 5
(Continued)

#	BAT Name[a]	R.A.[b]	Decl.	S/N	Counterpart Name	Other Name	Ctpt R.A.[c]	Ctpt Decl.	Flux[d]	Error	C[e]	Hrat[f]	Herr	Redshift[g]	Lum[h]	Type
476	SWIFT J2328.8+0331	352.199	3.517	5.04	NGC 7682		352.2664	3.5333	2.27		AB	0.35		0.0171	43.18	Sy2
477	"	"	"	"	NGC 7679		352.1944	3.5114	2.33		AB	0.35		0.0171	43.19	Sy1 / LIRG
478	SWIFT J2341.8+3033	355.447	30.567	6.69	UGC 12741		355.4811	30.5818	4.00	0.59		0.52	0.07	0.0174	43.44	Galaxy
479	SWIFT J2358.3+3337	359.577	33.609	4.85	SWIFT J2358.4+3339		359.6010	33.6420	2.08	0.61		0.42	0.10	?		

Notes.
[a] If a BAT name exists in the 9-month catalog (Tueller et al. 2008), then that name is used. If there is no 9-month BAT name, then the BAT name listed here is the name that was used to request XRT follow-up observations (and used in the HEASARC archive). When no previous BAT name for this source exists, we list here a BAT name derived from the BAT position in this catalog.
[b] The BAT source positions listed here are all uniformly generated from a blind search of the 22-month data and are J2000 coordinates.
[c] The counterpart position is the most accurate position known of the object in the "name" column in J2000 coordinates, and is usually taken from NED or SIMBAD. If no counterpart is known, the blind BAT position is listed.
[d] The flux is extracted from the BAT maps at the position listed for the counterpart, is in units of 10^{-11} erg $s^{-1}cm^{-2}$, and is computed for the 14–195 keV band.
[e] The meaning of the confusion flag is as follows: A: "Confused" source, B: "Confusing" source, AB: Both confused and confusing. To make sense of this confounding scenario, see Sections 4 and 4.3.
[f] The hardness ratio is the ratio of the 35–150 keV count rate to the 14–150 keV count rate.
[g] The redshifts are taken from the online databases NED and SIMBAD or in a few cases from our own analysis of the optical data. A blank indicates that the object is Galacatic, and a ? indicates that the object has an unknown redshift.
[h] The luminosity is computed from the flux and redshift in this table, with units of log[erg s^{-1}] in the 14–195 keV band.

References. Bikmaev et al. 2008, 2006; Bodaghee et al. 2006, 2007; Burenin et al. 2008; Butler et al. 2009; Chakrabarty et al. 2002; Coe et al. 1994; Homer et al. 2002; Israel et al. 2001; Juett & Chakrabarty 2005; Markwardt et al. 2005; Masetti et al. 2008, 2009; Rodriguez et al. 2009; Tomsick et al. 2008; Tueller et al. 2008; Walter et al. 2006; Wilson et al. 2003

(This table is also available in a machine-readable form in the online journal.)

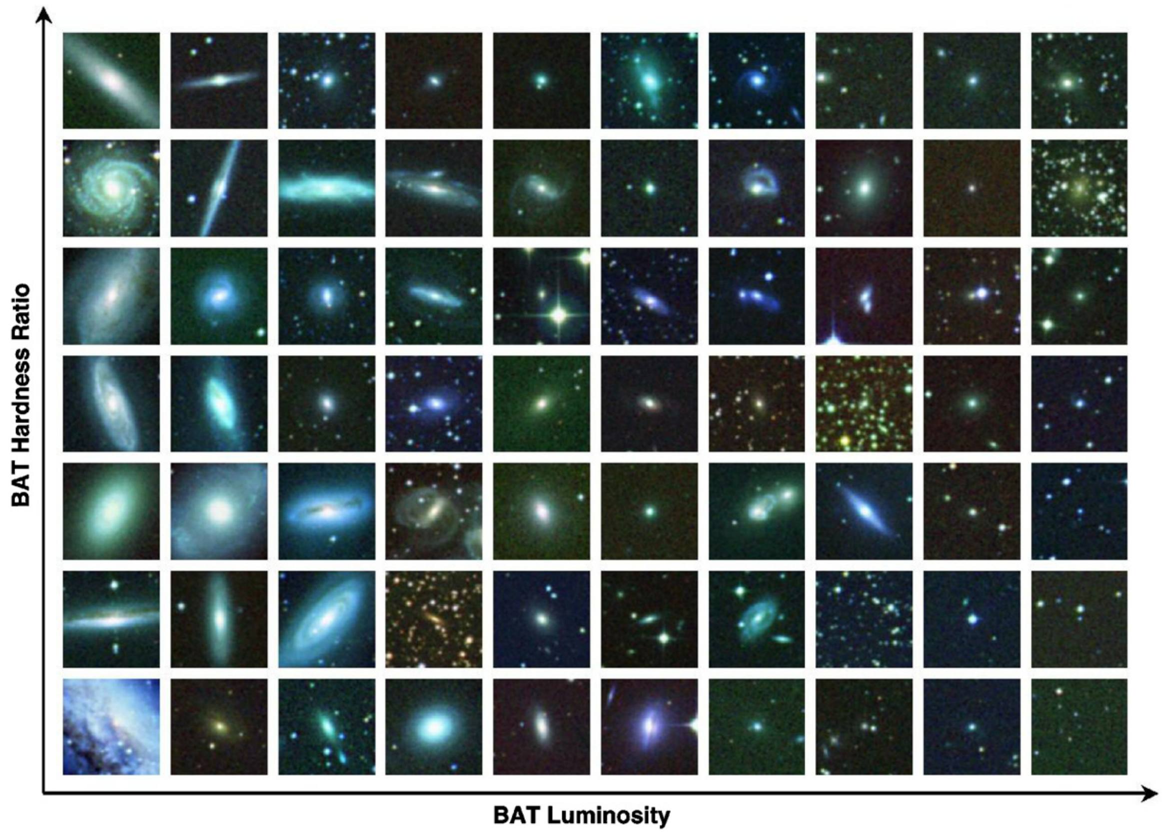

Figure 11. Typical host galaxies of BAT-detected Seyfert galaxies. The individual images are taken from the Palomar Digital Sky Survey, and are 2′ on a side. The BAT hardness-luminosity plane is divided into 70 bins, and a BAT source from that bin randomly selected to display.

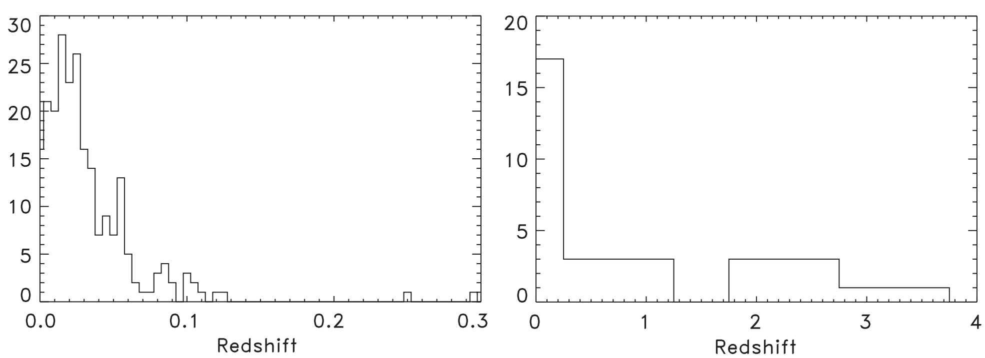

Figure 12. Histograms showing the redshift distribution of the AGN in the 22-month survey. The left panel shows the Seyfert distribution, and the right panel shows the beamed AGN distribution. The beamed AGN panel has redshift bins that are 0.5 units wide.

The BAT spectra of Cygnus A and Abell 2142 in the 14–100 keV band are dominated by the AGN component in or around the clusters. The other eight clusters are all hot ($kT \sim 10$ keV); their BAT spectra are consistent with an extension of the thermal emission modeled with ASCA/*XMM-Newton*/*Chandra* archival data in the 2–10 keV band and do not require any additional component for a good fit. In other words, there is no evidence of a non-thermal diffuse component in these clusters. We estimated the upper limit of the non-thermal emission by adding a power-law model to the spectral fit for the 10 detected clusters. The upper limit is $\sim 6\times10^{-12}$ erg cm^{-2} s^{-1} on average and the lower limit for the magnetic field B ranges from $\sim$0.2–1 μG, assuming inverse Compton scattering of Cosmic Microwave Background photons by relativistic electrons in the cluster. More details are described in the papers by Ajello et al. (2009a) and Okajima et al. (ApJ, submitted).

Some 20 sources are clearly identified, largely through follow-up *Swift*-XRT observations, with galaxies from which no sign of nuclear activity has yet been reported in other wavebands. Their mean luminosity is only slightly lower than that of those classed as Seyferts on the basis of optical spectra ($10^{43.53}$ compared with $10^{43.75}$ erg s^{-1}). These are probably low-z counterparts to the X-ray bright, optically normal (XBONG) sources discovered in the *Chandra* and *XMM-Newton* deep fields (Barger et al. 2005; Comastri et al. 2002).

5.3. Galactic Sources

5.3.1. X-ray Binaries

As can be seen from Table 5, approximately two-thirds of the Galactic sources are X-ray binaries. Of those whose nature is known, about 40% are high mass X-ray binaries, which reflects the BAT's sensitivity to hard-spectrum X-ray

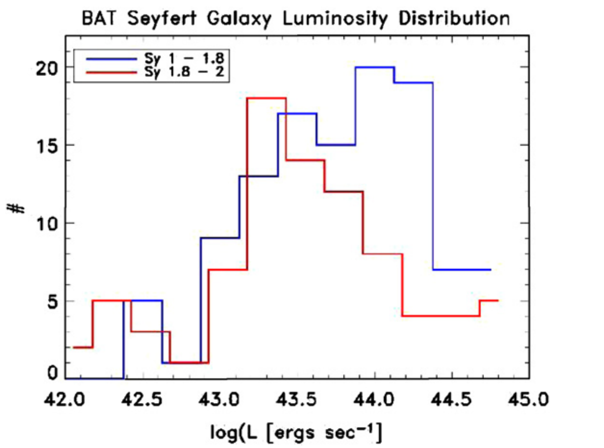

Figure 13. Distribution of Seyfert galaxy luminosities in the BAT 22-month survey.

sources. 60% are low mass X-ray binaries, which typically have softer spectra but can have a higher total flux. The low mass X-ray binary population is concentrated near the Galactic plane and bulge, whereas the high mass X-ray binary population is more distributed, including significant contributions from the Magellanic clouds.

The sensitivity of the survey is such that high luminosity sources ($>L_x \sim 10^{36}$ erg s^{-1}) are detectable anywhere in the Galaxy and the catalog is complete for sources that emit continuously at this level. However, since many X-ray binaries are transient it is likely that there are a significant number of additional X-ray binaries that are not seen in the present analysis (which is based on fluxes averaged over 22 months), but that can be detected in specific shorter intervals. This will be the subject of further work. The detection of outbursts from transients that do not repeat, or that repeat only on timescales of several years, should scale approximately linearly with the length of the survey.

5.3.2. CVs and Other Accreting White Dwarf Systems

Accreting white dwarf binaries constitute the second most common category of Galactic sources. Of these, 31 have been identified as CVs or CV candidates. Of the 31 CVs detected with BAT, 14 are in the Barlow et al. (2006) (*INTEGRAL*) list, while 17 are new detections in hard X-ray surveys. Because the *INTEGRAL* catalog goes deeper near the Galactic plane but the BAT catalog is more sensitive at higher latitude, the lists of CVs in the two catalogs are complementary. With the expanded list, we confirm that the hard X-ray-selected CVs are dominated by magnetic CVs of the intermediate polar (IP) subtype, also known as DQ Her type stars (see also Brunschweiger et al. 2009).

In addition, four hard X-ray bright symbiotic stars have been detected by BAT, as summarized by Kennea et al. (2007), and there is now a candidate to be the fifth member of the class. Finally, BAT has also detected one Be star, gam Cas, for which an accreting white dwarf companion is one of the three possibilities proposed as the origin of the X-ray emission (Kubo et al. 1998).

5.3.3. SNRs and Non-Accretion Powered Pulsars

We detect hard X-ray emission from eight pulsars and/or their associated Pulsar Wind Nebula (PWN) or supernova remnants (SNRs). Our upper limit on PSR J1846−0258 is consistent with the flux level at which it was detected in a long *INTEGRAL*-IBIS observation and reported in Bird et al. (2007). In the case of HESS J1813−178, it appears that we are detecting emission that is from the point source seen at lower energies (Funk et al. 2007) rather than directly related to the slightly extended VHE gamma-ray emission. The only SNR-related source that is not associated with a PWN is Cas A.

5.3.4. The Galactic Center

Because of the limited resolution of the BAT instrument the emission reported as from Sgr A* should be regarded as the net emission from a region of $\sim 6'$ radius centered on the Galactic center. It is possible that a number of sources contribute.

6. CONCLUSIONS

The 22 month BAT catalog reinforces and enhances the results from the 3 month (Markwardt et al. 2005) and 9 month (Tueller et al. 2008) catalogs and shows that the BAT survey continues to increase in sensitivity roughly as the square root of time and is far from being confusion or systematics limited. Future papers will discuss the X-ray spectral and timing properties of these sources as well as the nature of the optical identifications, in a manner similar to that of Winter et al. (2008, 2009). We have also obtained extensive optical imaging and spectroscopy of the AGN population (Winter et al. 2009), more detailed X-ray observations as well as *Spitzer* IR spectroscopy (Melendez et al. 2009) and radio data which will be presented in future publications. These results will allow the first large-scale categorization of the AGN phenomenon from a large uniform and unbiased sample as well as a detailed comparison with results obtained with other selection techniques.

REFERENCES

Ajello, M., et al. 2009a, ApJ, 690, 367
Ajello, M., et al. 2009b, ApJ, 699, 603
Barger, A. J., Cowie, L. L., Mushotzky, R. F., Yang, Y., Wang, W.-H., Steffen, A. T., & Capak, P. 2005, AJ, 129, 578
Barlow, E. J., Knigge, C., Bird, A. J., J Dean, A., Clark, D. J., Hill, A. B., Molina, M., & Sguera, V. 2006, MNRAS, 372, 224
Barthelmy, S. D., Cline, T. L., Butterworth, P., Kippen, R. M., Briggs, M. S., Connaughton, V., & Pendleton, G. N. 2000, in AIP Conf. Proc. 526, Gamma-ray Bursts, 5th Huntsville Symp., ed. R. M. Kippen, R. S. Mallozzi, & G. J. Fishman (Melville, NY: AIP), 731
Barthelmy, S. D., et al. 2005, Space Sci. Rev., 120, 143
Bartlett Lyle. PhD thesis, Astronomy Department, University of Maryland College Park
Beckmann, V., Gehrels, N., Shrader, C. R., & Soldi, S. 2006, ApJ, 638, 642
Beckmann, V., et al. 2009, A&A, 505, 417
Bikmaev, I. F., Sunyaev, R. A., Revnivtsev, M. G., & Burenin, R. A. 2006, Astron. Lett., 32, 221
Bikmaev, I. F., Burenin, R. A., Revnivtsev, M. G., Sazonov, S. Y., Sunyaev, R. A., Pavlinsky, M. N., & Sakhibullin, N. A. 2008, Astron. Lett., 34, 653
Bodaghee, A., Walter, R., Zurita Heras, J. A., Bird, A. J., Courvoisier, T. J.-L., Malizia, A., Terrier, R., & Ubertini, P. 2006, A&A, 447, 1027
Bodaghee, A., et al. 2007, A&A, 467, 585
Bird, A. J., et al. 2007, ApJS, 170, 175
Brunschweiger, J., Greiner, J., Ajello, M., & Osborne, J. 2009, A&A, 496, 121
Burenin, R. A., Mescheryakov, A. V., Revnivtsev, M. G., Sazonov, S. Y., Bikmaev, I. F., Pavlinsky, M. N., & Sunyaev, R. A. 2008, Astron. Lett., 34, 367
Burrows, D. N., et al. 2005, Space Sci. Rev., 120, 165
Butler, S. C., et al. 2009, ApJ, 698, 502
Caroli, E., Stephen, J. B., Spizzichino, A., di Cocco, G., & Natalucci, L. 1986, in Ettore Majorana Int. Science Ser., Data Analysis in Astronomy II, ed. V. Di Ges, L. Scarsi, P. Crane, J. H. Friedman, & S. Levialdi (New York: Plenum), 77
Chakrabarty, D., Wang, Z., Juett, A. M., Lee, J. C., & Roche, P. 2002, ApJ, 573, 789
Coe, M. J., et al. 1994, MNRAS, 270, L57

Comastri, A., et al. 2002, ApJ, 571, 771
Falanga, M., Belloni, T., & Campana, S. 2006, A&A, 456, L5
Fenimore, E. E., & Cannon, T. M. 1981, Appl. Opt., 20, 1858
Fiore, F., Guainazzi, M., & Grandi, P. SAX Cookbook, http://heasarc.gsfc.nasa.gov/docs/sax/abc/saxabc/saxabc.html
Forman, W., Jones, C., Cominsky, L., Julien, P., Murray, S., Peters, G., Tananbaum, H., & Giacconi, R. 1978, ApJS, 38, 357
Funk, S., et al. 2007, A&A, 470, 249
Gehrels, N., et al. 2004, ApJ, 611, 1005
Gilli, R., Comastri, A., & Hasinger, G. 2007, A&A, 463, 79
Homer, L., Anderson, S. F., Margon, B., Downes, R. A., & Deutsch, E. W. 2002, AJ, 123, 3255
Ibarra, A., et al. 2009, A&A, 497, L5
Israel, G. L., et al. 2001, A&A, 371, 1018
Jourdain, E., Götz, D., Westergaard, N. J., Natalucci, L., & Roques, J. P. 2008, Proceedings of the 7th INTEGRAL Workshop, 2008 September 8–11, Copenhagen, Denmark. Online at http://pos.sissa.it/cgi-bin/reader/conf.cgi?confid=67, 144
Jourdain, E., & Roques, J. P. 2008, in Proceedings of the 7th INTEGRAL Workshop, 2008 September 8–11, Copenhagen, Denmark. Online at http://pos.sissa.it/cgi-bin/reader/conf.cgi?confid=67, 143
Juett, A. M., & Chakrabarty, D. 2005, ApJ, 627, 926
Kennea, J. A., Mukai, K., Tueller, J., Sokoloski, J., Luna, J., Burrows, D., & Gehrels, N. 2007, BAAS, 38, 149
Krimm, H., et al. 2006, ATel, 904, 1
Krivonos, R., Revnivtsev, M., Lutovinov, A., Sazonov, S., Churazov, E., & Sunyaev, R. 2007, A&A, 475, 775
Kubo, S., Murakami, T., Ishida, M., & Corbet, R. H. D. 1998, PASJ, 50, 417
Levine, A. M., et al. 1984, ApJS, 54, 581
Markwardt, C. B., Tueller, J., Skinner, G. K., Gehrels, N., Barthelmy, S. D., & Mushotzky, R. F. 2005, ApJ, 633, L77
Masetti, N., et al. 2008, A&A, 482, 113
Masetti, N., et al. 2009, A&A, 495, 121
Melendez, M., et al. 2009, BAAS, 41, 239
Olive, J.-F., et al. 2003, in AIP Conf. Proc. 662, Gamma-Ray Burst and Afterglow Astronomy 2001: A Workshop Celebrating the First Year of the HETE Mission, ed. G. R. Ricker & R. K. Vanderspek (Melville, NY: AIP), 88
Reig, P., Belloni, T., Israel, G. L., Campana, S., Gehrels, N., & Homan, J. 2008, A&A, 485, 797
Revnivtsev, M., Sazonov, S., Jahoda, K., & Gilfanov, M. 2004, A&A, 418, 927
Rodriguez, J., Tomsick, J. A., & Chaty, S. 2009, A&A, 494, 417
Roming, P. W. A., et al. 2005, Space Sci. Rev., 120, 95
Skinner, G. K. 1995, Exp. Astron., 6, 1
Skinner, G. K. 2008, Appl. Opt., 47, 2739
Steiner, J. E., Cieslinski, D., & Jablonski, F. J. 1988, in ASP Conf. Ser. 1, Progress and Opportunities in Southern Hemisphere Optical Astronomy, The CTIO 25th Anniversary Symposium, ed. V. M. Blanco & M. M. Phillips (San Francisco, CA: ASP), 67
Thorstensen, J. R., Peters, C. S., Sheets, H. A., & Skinner, J. N. 2009, BAAS, 41, 468
Tomsick, J. A., Chaty, S., Rodriguez, J., Walter, R., & Kaaret, P. 2008, ApJ, 685, 1143
Treister, E., Urry, C. M., & Virani, S. 2009, ApJ, 696, 110
Tueller, J., Mushotzky, R. F., Barthelmy, S., Cannizzo, J. K., Gehrels, N., Markwardt, C. B., Skinner, G. K., & Winter, L. M. 2008, ApJ, 681, 113
Walter, R., et al. 2006, A&A, 453, 133
Wilson, C. A., Patel, S. K., Kouveliotou, C., Jonker, P. G., van der Klis, M., Lewin, W. H. G., Belloni, T., & Méndez, M. 2003, ApJ, 596, 1220
Winter, L. M., Mushotzky, R. F., Reynolds, C. S., & Tueller, J. 2009, ApJ, 690, 1322
Winter, L. M., Mushotzky, R. F., Tueller, J., & Markwardt, C. 2008, ApJ, 674, 686